IVYSPRING INTERNATIONAL PUBLISHER

Theranostics

2027; 17(1): 524-550. doi: 10.7150/thno.138957

Research Paper

Therapeutic decoupling of restenosis prevention from impaired vascular healing with regenerative nanovesicle-eluting bioresorbable scaffolds

Min-Kyu Kang[1,†], Ji Won Kim[2,3,†], Yu-Jeong Lee[1,†], Dong-Sung Won[2,3], Gi Wook Lee[4], Weiqiang Liu[5], Chae-lin Kim[6], Su-Hyun Park[1], Ju-El Kim[1], Tae-Hyun Heo[1], Seung Jin Eo[2,3], Gun-Jae Jeong[7], Ilkoo Noh[8,9], Min-Ho Kang[10], Han Young Kim[10], Young Min Shin[11], Jung Bok Lee[12], Minseo Park[6], Hyun-Ji Park[6], Rosaire Mongrain[5], Hyung Il Kim[4], Jung-Hoon Park[2,3,✉], Jeong-Kee Yoon[1,✉]

1. Department of Systems Biotechnology, Chung-Ang University, Anseong-Si, Gyeonggi-Do 17546, Republic of Korea.
2. Biomedical Engineering Research Center, Asan Institute for Life Sciences, Asan Medical Center, Seoul 05505, Republic of Korea.
3. Department of Convergence Medicine, Asan Medical Center, University of Ulsan College of Medicine, Seoul 05505, Republic of Korea.
4. Dotter Co. Ltd., Incheon 22007, Republic of Korea.
5. Department of Mechanical Engineering, McGill University, Montréal, QC, H3A 0C3, Canada.
6. Department of Molecular Science and Technology, Ajou University, Suwon 16499, Republic of Korea.
7. School of Nanomedical Engineering, Korea National University of Transportation, Chungju-si, Chungbuk 27469, Republic of Korea.
8. Department of Biomedical Technology, Kangwon National University, Chuncheon 24341, Republic of Korea.
9. Institute of Bioscience & Biotechnology, Kangwon National University, Chuncheon 24341, Republic of Korea.
10. Department of Biomedical-Chemical Engineering, The Catholic University of Korea, Bucheon-si, Gyeonggi-do, Republic of Korea.
11. Institute of Cell and Tissue Engineering, College of Medicine, The Catholic University of Korea, Seoul 06591, Republic of Korea.
12. Department of Biological Science, Research Institute of Women's Health, Brain Korea 21 Project, Sookmyung Women's University, Seoul 04310, Republic of Korea.

† These authors contributed equally to this work as co-first authors.

✉ Corresponding authors: Jeong-Kee Yoon, Ph.D. (E-mail: jyoon342@cau.ac.kr). Jung-Hoon Park, Ph.D. (E-mail: jhparkz@amc.seoul.kr).

© 2027 The Author(s). This is an open access article distributed under the Creative Commons Attribution 4.0 International Licence, subject to the Publisher's Terms of Use at https://ivyspring.com/terms.

Received: 2026.06.06; Accepted: 2026.10.12; Published: 2027.01.01

Abstract

Background: Stent-based revascularization remains limited by the competing demands of restenosis prevention and vascular healing. Although drug-eluting stents reduce neointimal hyperplasia by suppressing vascular smooth muscle cell (VSMC) proliferation, their cytostatic mechanisms can delay re-endothelialization and compromise vascular repair. This unresolved therapeutic tradeoff underscores the need for a regenerative scaffold strategy that preserves antirestenotic efficacy while actively restoring vascular healing.

Methods: We developed a nanovesicle-eluting bioresorbable scaffold (NVE-BRS) by non-covalently loading MSC-derived nanovesicles (MSC-NVs) onto a PMB30W-functionalized, honeycomb-structured thin-strut PLLA scaffold, followed by lyophilization for off-the-shelf use. Lyophilization stability, coating and release behavior, shear retention, NV diffusion, radial expansion mechanics, *in vitro* vasculomodulatory activity, and *in vivo* efficacy were evaluated using computational analyses, vascular cells and a balloon-injured rabbit iliac artery model with angiography, OCT, histology, and immunofluorescence.

Results: The PMB30W-based amphiphilic interface enabled uniform non-covalent MSC-NV loading and localized release without chemical conjugation, while lyophilization preserved EV-mimetic morphology, particle and cargo profiles, and bioactivity. Computational analyses supported transmural NV delivery and scaffold mechanical integrity after expansion. *In vitro*, MSC-NVs promoted endothelial recovery and angiogenic activity while suppressing VSMC inflammatory activation, proliferation, and pro-atherogenic macrophage responses. *In vivo*, NVE-BRS maintained vascular patency and reduced neointimal thickness from 0.40 ± 0.02 mm to 0.17 ± 0.01 mm and stenosis area from 48.8 ± 1.56% to 19.38 ± 1.67% compared with bare BRS. Histology further showed increased CD31-positive endothelial coverage and reduced VCAM-1, PDGFR-β, α-SMA, and CD68 signals.

Conclusion: NVE-BRS establishes an off-the-shelf regenerative scaffold platform that enables therapeutic decoupling between antirestenotic efficacy and vascular healing through coordinated endothelial repair, suppression of VSMC activation, and inflammatory modulation.

Keywords: anti-restenosis, bioresorbable scaffold, extracellular vesicles, mesenchymal stem cells-derived nanovesicles, vasculoregeneration

Introduction

Atherosclerosis is the underlying pathological process of multiple cardiovascular diseases and a leading cause of global mortality [1-5]. Progressive arterial plaque formation narrows the lumen and impairs blood flow, often necessitating revascularization to restore perfusion. Although pharmacological therapy slows disease progression, patients with obstructive lesions ultimately require interventional treatment [6]. Coronary artery bypass grafting (CABG) and percutaneous coronary intervention (PCI) are the primary therapeutic options for restoring coronary blood flow. Although PCI is less invasive and offers faster recovery than CABG, stent implantation remains associated with restenosis [7, 8]. Bare-metal stents (BMSs) release metal ions that induce hypersensitivity reactions, triggering foreign body responses, impaired re-endothelialization, and vascular smooth muscle cell (VSMC) activation that induce neointimal hyperplasia [9]. These limitations led to the development of drug-eluting stents (DESs), which locally release antiproliferative agents to prevent abnormal VSMC growth for prolonged patency. Although DESs substantially reduce early restenosis, their cytostatic agents delay stent surface re-endothelialization, leading to late thrombosis and late-stage restenosis [8, 10, 11]. To address these challenges, polymer-based bioresorbable scaffolds (BRSs) have emerged as next-generation platforms to reduce late restenosis while enabling diverse surface-modification strategies that promote rapid and functional re-endothelialization [12-14].

Mesenchymal stem cells (MSCs) are widely investigated as a promising cell therapy owing to their capacity to modulate immune responses, inhibit apoptosis, and promote tissue regeneration via paracrine mechanisms [15-18]. However, clinical translation of MSC-based therapies is limited to poor *in vivo* persistence, inefficient targeting, time- and resource-intensive nature of cell preparation, and risks of unpredictable biological behavior inducing off-target effects [17, 19, 20]. Accordingly, MSC-derived small extracellular vesicles (EVs) (i.e., exosomes) have emerged as cell-free therapeutic alternatives that retain anti-inflammatory and pro-regenerative functions, while providing a nanoscale platform compatible with long-term storage and off-the-shelf use [21-24]. MSCs, MSC-derived exosomes, and their mimetics, such as artificial nanovesicles (MSC-NVs) synthesized by physical extrusion of live MSCs for increased productivity, have demonstrated therapeutic potential in vascular diseases [25, 26]. However, their application to stent-based revascularization strategies remain limited. Direct coating of viable cells onto stent surfaces presents substantial technical and translational challenges, including poor cell retention under physiological shear stress, short shelf life, and incompatibility with large-scale manufacturing and sterilization. Although exosome- and NV-based approaches provide cell-free alternatives, stable integration onto stent platforms requires long-term stabilization via lyophilization, for which systematic studies on bioactivity preservation and release remain limited [27]. Moreover, while MSC-derived paracrine signaling is known to support endothelial repair, its effects on VSMCs are inconsistent, raising concerns regarding unintended activation and promotion of neointimal hyperplasia [28, 29]. Collectively, these biological ambiguities and translational constraints have hindered the adoption of MSC-based and MSC-derived therapies in anti-restenotic stent platforms.

In this study, we address these unresolved biological and translational challenges by developing a vasculomodulatory MSC-NV-eluting BRS (NVE-BRS) **(Figure S1)**. A biodegradable polymer-based BRS was functionalized with an amphiphilic polymer to form a stable MSC-NV interface on its surface. *In vitro* and *in vivo* studies demonstrate that MSC-NV or NVE-BRS regulates vasculomodulation, by promoting re-endothelialization while suppressing VSMC activation and inflammatory responses, overcoming limitations of conventional DES. Efficient delivery to the intima and media was enabled by the synergistic interplay between BRS architecture and the intrinsic transcytotic capability of MSC-NVs, supported by computational analysis and their EV-mimetic properties. Notably, MSC-NVs retained therapeutic efficacy following lyophilization, indicating that bioactivity was maintained along with the translational feasibility of the NVE-BRS platform for long-term storage and manufacturing. This work advances regenerative and clinically translatable precision vascular therapies by integrating clinically relevant bioactive NVs with the structural and chemical features of BRS to enable efficient delivery and balanced vascular repair.

Results and Discussion

Preparation and characterization of MSC-NVs and NVE-BRS

MSC-NVs were produced via serial extrusion through membranes with pore sizes of 10, 5, and 0.4 μm **(Figure 1A)**. NVE-BRSs were prepared via sequential coating with poly(2-methacryloyloxyethyl phosphorylcholine-co-n-butyl methacrylate) (PMB30W) and MSC-NVs, followed by lyophilization and crimping for further experiments. Before *in vivo*

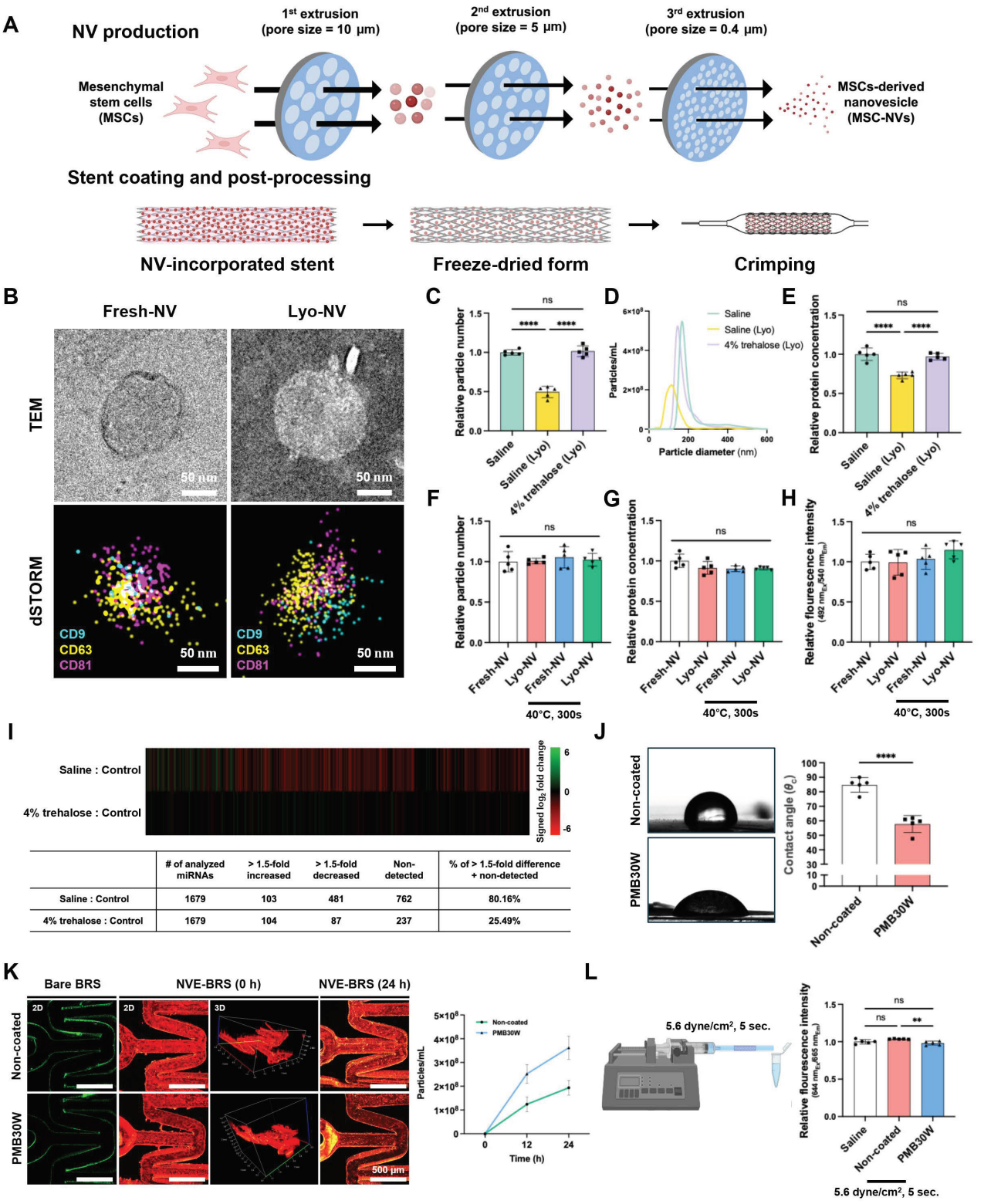
use, NVE-BRSs underwent lyophilization to facilitate stable delivery and long-term storage. To enhance MSC-NV stability during lyophilization, 4% trehalose was added as a cryoprotectant. Both fresh (Fresh-NVs) or lyophilized MSC-NVs (Lyo-NVs) exhibited diameters of approximately 100 nm, confirmed by transmission electron microscopy (TEM) and direct stochastic optical reconstruction microscopy (dSTORM) imaging **(Figure 1B)**. dSTORM imaging further verified the presence of tetraspanin markers, including CD9, CD63, and CD81, supporting their EV-mimetic identity. Lyophilization in the presence of 4% trehalose preserved NV morphology, particle size, and surface protein distribution without significant differences from fresh-NVs. Consistently, nanoparticle tracking analysis (NTA) and bicinchoninic acid (BCA) assay results showed that particle concentration **(Figure 1C)**, particle size distribution **(Figure 1D)**, and protein concentration **(Figure 1E)** were maintained after lyophilization with 4% trehalose. In addition, thermal stability of Lyo-NVs was evaluated via heat treatment at 40 °C for 300 s, reflecting thermal stress during crimping. Fresh-NVs in suspension or Lyo-NVs in powder form exhibited no significant changes in total particle concentration (**Figure 1F**), protein content **(Figure 1G)**, and intravesicular RNA quantity **(Figure 1H)**. Moreover, microarray analysis revealed that 4% trehalose minimized lyophilization-induced alterations in intravesicular microRNA (miRNA) content **(Figure 1I)**.

The BRS surface was modified with the amphiphilic coating agent PMB30W to reduce its intrinsic hydrophobicity, confirmed via contact angle measurement **(Figure 1J)**. To determine the MSC-NV concentration for BRS coating, BRSs were treated with DiD-labeled MSC-NV solutions at 400, 700, and 1,000 μg/mL. The DiD-positive coating area was significantly lower at 400 μg/mL than at 700 and 1,000 μg/mL, whereas no significant difference was observed between 700 and 1,000 μg/mL **(Figure S2)**. Thus, 700 μg/mL (1.19×10^{11} particles/mL) was selected as the coating concentration for subsequent NVE-BRS preparation. Both uncoated (non-coated) and PMB30W-coated stents (PMB30W) showed a uniform and continuous NV layer, confirmed via confocal imaging, without significant differences in the adsorbed MSC-NV amount **(Figure 1K)**. However, we hypothesized that hydrophilic surfaces form a stable hydration layer that limits direct interfacial contact of BRS and MSC-NVs, reducing adhesion strength and facilitating adsorbed NV release. Consistent with our hypothesis, static release testing showed increased NV release in the PMB30W group compared with the non-coated group **(Figure 1K)**. MSC-NV coating stability was evaluated under simulated blood flow by applying a shear stress of 5.6 dyne/cm² for 5 s using a syringe pump. The coating remained intact without detectable damage under this short-term dynamic condition **(Figure 1L)**.

Overall, these findings showed that adding 4% trehalose during lyophilization preserves the key physicochemical properties of MSC-NVs. Maintenance of morphology, surface marker distribution, protein content, particle concentration, and intravesicular RNA after lyophilization and heat exposure indicated stability under storage-related stress and transient thermal loads during stent crimping. Notably, reduced miRNA alterations in the 4% trehalose group suggested that trehalose stabilizes both vesicle structure and cargo, which may help maintain MSC-NV bioactivity. In addition, the NV coating remained stable under the tested flow condition (5.6 dyne/cm² for 5 s), supporting short-term resistance to shear-induced detachment. However, the applied shear stress and exposure duration were lower than typical arterial conditions, requiring additional *in vivo* evaluation of coating stability. Existing stent-based EV delivery strategies predominantly depend on chemical conjugation, restricting vesicle release and introducing translational barriers due to additional chemical modification steps [30, 31]. In contrast, this platform used a PMB30W coating layer, a biocompatible amphiphilic polymer, to alter surface hydrophilicity and enable simple NV adsorption and localized delivery [32-34]. Combined with preserved functionality after lyophilization, this strategy supports a manufacturing-compatible approach with translational potential for next-generation EV-eluting stent systems.

Numerical simulation for NV diffusion

The integrated computational framework used to evaluate NV transport and stent mechanics is summarized in **Figure 2A**. The mass transport model was constructed using a half-artery domain, with the stent surface defined as the drug-release boundary, whereas the structural model was used to simulate radial stent expansion under internal pressure. The temporal evolution of drug concentration was strongly influenced by the assigned diffusion coefficient (D). Our simulative results demonstrate that the lower-diffusivity case maintained a higher mean normalized concentration over the 28-day period, indicating slower transport and prolonged local retention, while higher diffusivity promoted more rapid redistribution and clearance of the released NVs, leading to a faster reduction in mean concentration **(Figure 2B)**. These results indicate that the diffusion coefficient is a key parameter governing the balance between local drug retention and spatial redistribution within the arterial wall tissue.



	# of analyzed miRNAs	> 1.5-fold increased	> 1.5-fold decreased	Non-detected	% of > 1.5-fold difference + non-detected
Saline : Control	1679	103	481	762	80.16%
4% trehalose : Control	1679	104	87	237	25.49%

Figure 1. MSC-NV and NVE-BRS preparation and characterization. (A) Schematic illustration of MSC-NV preparation via serial extrusion using membranes with pore sizes of 10, 5, and 0.4 μm, followed by incorporation onto BRS surfaces. (B) TEM and dSTORM images of MSC-NVs with and without lyophilization. Scale bar = 50 nm. (C-E) Particle stability evaluation following lyophilization with 4% trehalose supplementation. (C) Relative particle number (n = 5), (D) particle size distribution, and (E) relative MSC-NV protein concentration (n = 5). (F-H) MSC-NV thermal stability during stent crimping (40 °C, 300 s). (F) Relative particle number (n = 5), (G) relative protein concentration (n = 5), and (H) relative fluorescence intensity of intravesicular RNA (n = 5). (I) Comparison of miRNA expression profiles among fresh MSC-NVs (control), lyophilized MSC-NVs without trehalose (saline), and lyophilized MSC-NVs with 4% trehalose. (J) Wettability analysis of stent surfaces (n = 5). (K) Representative 2D and 3D images of non-coated and PMB30W-coated stents with or without NV coating (Bare BRS and NVE-BRS), with NVE-BRS shown at 0 and 24 h. Quantification of released NVs from non-coated and PMB30W-coated stents (n = 9). Scale bar = 500 μm. (L) Shear stress test under flow (5.6 dyne/cm², 5 s) showed no detectable loss of MSC-NV coating on PMB30W-coated stents compared with non-coated stents (n = 5). Quantitative data are expressed as the mean ± standard deviation (SD). Statistical significance was determined using an unpaired two-tailed Student's t-test for comparisons between two groups and one-way analysis of variance (ANOVA) followed by Tukey's multiple comparisons test for comparisons among more than two groups. ns = non-significant, $^{**}p < 0.01$, $^{****}p < 0.0001$.

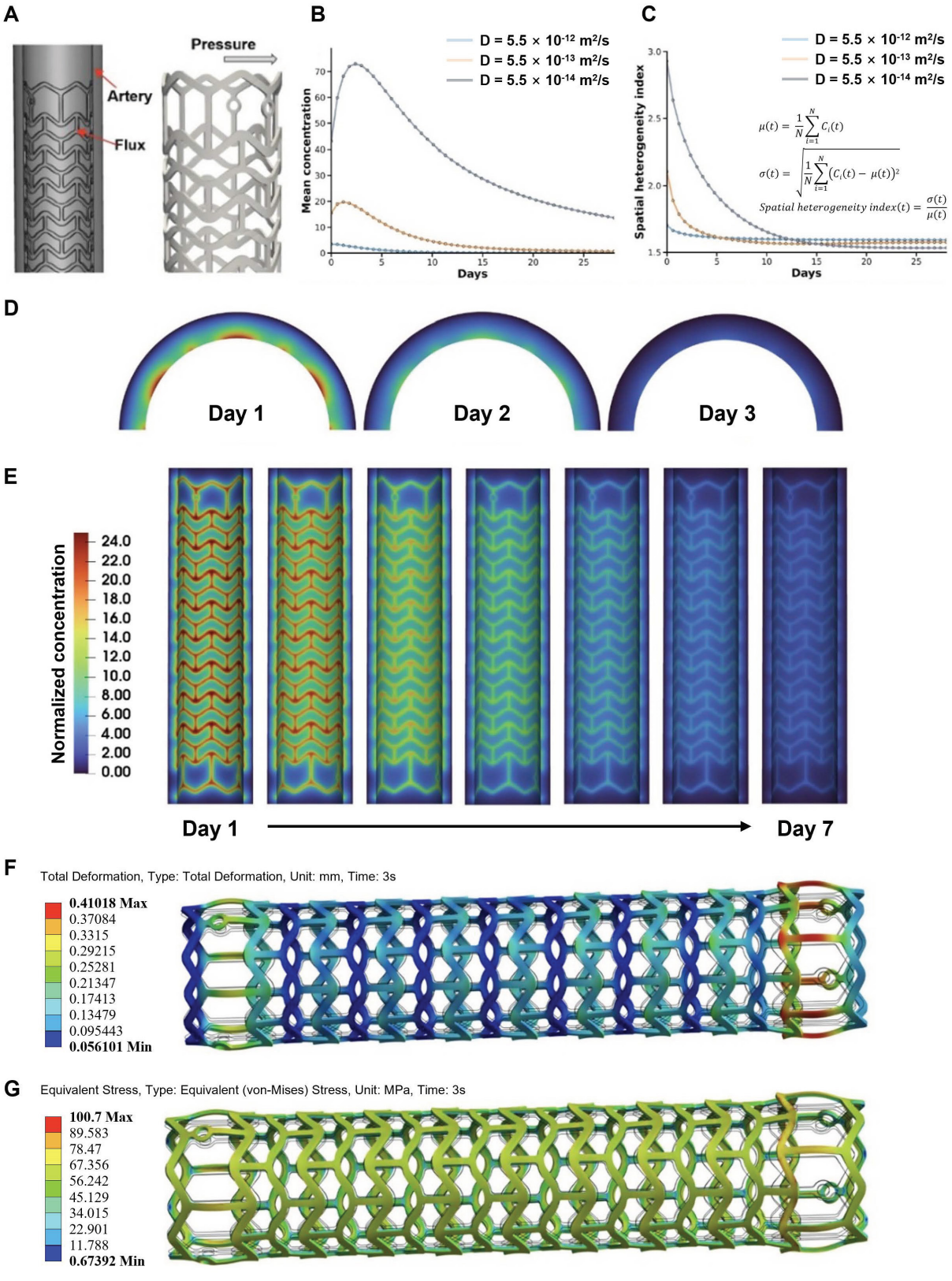


Figure 2. Computational evaluation of NV delivery and structural BRS mechanics. (A) Simulation setup illustrating the mass transport in half of the artery (left) and the structural expansion under internal radial pressure (right). (B) Mean normalized concentration over 28 days for D = 5.5 × 10^{-12}, 5.5 × 10^{-13}, and 5.5 × 10^{-14} m^2/s, showing the effect of diffusivity on drug concentration evolution. (C) Spatial heterogeneity index over 28 days for different diffusion coefficients, showing progressive homogenization of MSC-NV distribution within the arterial wall over time. (D) Cross-sectional concentration contours showing radial transmural drug diffusion over time. (E) Front-view concentration contours illustrating temporal drug distribution along the stent surface, including local accumulation near struts and progressive spatial redistribution. Panels D and E share the same color scale for normalized concentration. (F) Contour plot of total structural deformation under 2.5 MPa internal pressure. (G) Contour plot of equivalent von Mises stress.

In addition to the diffusivity-dependent concentration response, spatial heterogeneity of MSC-NV distribution within the arterial wall was quantitatively evaluated using the spatial heterogeneity index **(Figure 2C)**. Lower diffusion coefficients exhibited higher initial heterogeneity, indicating localized accumulation of MSC-NVs near the stent surface, whereas higher diffusivity promoted more rapid spatial homogenization over time. In all conditions, the heterogeneity index gradually decreased during the 28-day simulation period, reflecting progressive redistribution of MSC-NVs throughout the arterial wall tissue. These findings suggest that diffusion coefficient strongly influences not only overall concentration retention but also the spatial uniformity of NV exposure within the vessel wall. The contour plots obtained at $D = 5.5 \times 10^{-12}$ m²/s further illustrate the spatial evolution of NV transport. The cross-sectional views show the radial distribution of drug concentration across the arterial wall at different time points **(Figure 2D)**. The concentration was initially localized near the stent-facing region, became more spatially distributed across the arterial wall as diffusion progressed, and subsequently decreased as the released drug was depleted over time. Notably, the concentration had already decreased substantially by day 7, although the full transient simulation was performed over a 28-day period. The front-view contours show the corresponding temporal diffusion pattern along the stent surface **(Figure 2E)**. These views demonstrate that the drug released from the stent initially accumulated around the stent struts and subsequently spread along the arterial surface, while the overall concentration intensity gradually diminished. Since panels D and E share the same color scale, the temporal changes in concentration magnitude and spatial redistribution can be directly compared.

Together, these results suggest that MSC-NV delivery from NVE-BRS is governed by both diffusivity and spatial proximity to the strut surface. Lower diffusion coefficients favor prolonged local retention, whereas higher diffusion coefficients enhance spatial spreading and more rapidly reduce concentration gradients. This trade-off is important for optimizing stent-based drug delivery, where sufficient local retention is required for therapeutic efficacy, while excessive localization may result in nonuniform tissue exposure. A limitation of this analysis is that the diffusion coefficient was adopted from literature values reported for nanoparticles of comparable dimensions [35]. This approach also implicitly assumes that NV diffusion occurs through a homogeneous medium without anisotropy and that the NV transport process is Fickian, without reaction or entrapment. In other words, all NVs were assumed to diffuse through the different media. In addition, depletion of NVs in the carrier was modeled based on prior molecular depletion behavior of compounds with similar diffusion properties. Future work should address the experimental characterization of the NV transport process using a Franz cell system with vascular tissue to obtain a more precise estimate of the diffusion coefficient.

Structural response of BRS to radial expansion

Under an internal inflation pressure of 2.5 MPa, corresponding to approximately 25 atm, the poly(L-lactic acid) (PLLA)-based BRS underwent radial expansion with a complex three-dimensional deformation pattern. The mechanical response was evaluated using equivalent von Mises stress, which provides a scalar representation of the multiaxial stress state and enables assessment of yielding and plastic deformation. The total deformation contour indicates a maximum displacement of approximately 0.41 mm **(Figure 2F)**. The deformation pattern demonstrates overall radial expansion of the scaffold, with slightly greater displacement near the longitudinal ends. This behavior is consistent with the dogboning deformation commonly observed during balloon-driven stent deployment.

The von Mises stress distribution indicates a maximum stress of approximately 100.7 MPa, exceeding the initial tensile yield strength of PLLA, 66.5 MPa **(Figure 2G)**. This result suggests that localized plastic deformation occurred during balloon expansion, allowing the scaffold to retain its expanded configuration after deflation and provide mechanical support to the arterial wall. The highest stresses were observed near the U-shaped crowns and connecting struts, where deformation was primarily accommodated during deployment. The asymmetric scaffold design may also provide recognizable structural landmarks under imaging, thereby facilitating stent orientation and image-guided navigation.

In vitro re-endothelialization and endothelial protective effects of MSC-NVs

Rapid re-endothelialization after stent implantation is essential for restoring vascular homeostasis and maintaining long-term vessel patency. However, the post-implantation microenvironment is highly inflammatory, impairing endothelial cell (EC) migration and delaying endothelial recovery. In addition, mTOR inhibitors such as sirolimus or everolimus in DESs also exert antiproliferative, anti-migrative, and cytotoxic effects

on ECs, hindering re-endothelialization [36-38]. Therefore, strategies that simultaneously promote EC recovery and modulate the inflammatory vascular environment are required for preventing late-stage restenosis. Thus, MSC-NVs were used *in vitro* to confirm their anti-inflammatory and pro-endothelial recovery functions and to compare the therapeutic efficacy of Fresh- and Lyo-NVs. The endothelial recovery effects of MSC-NVs were evaluated by inducing inflammatory dysfunction in human coronary artery endothelial cells (hCAECs) via lipopolysaccharide (LPS) stimulation (100 ng/mL).

Based on dose-dependent assessments of inflammatory regulation, metabolic activity, and cytotoxicity, 10 μg/mL (1.70×10^9 particles/mL) was selected for subsequent *in vitro* experiments. In LPS-stimulated hCAECs, Fresh- and Lyo-NVs generally reduced inflammatory and endothelial dysfunction marker expression across concentrations of 0.1–50 μg/mL, with robust effects at 10 μg/mL and limited or variable additional benefit at 50 μg/mL. CCK-8 analysis further showed recovery of LPS-reduced metabolic activity, while NV-only Live/Dead imaging showed no overt cytotoxicity up to 50 μg/mL **(Figure S3)**. Time-course analysis showed that cell-associated DiD fluorescence from both Fresh- and Lyo-NVs progressively increased in hCAECs over 0–24 h, with the highest fluorescence observed at 24 h **(Figure 3A)**. Endothelial dysfunction is accompanied by the upregulation of pro-inflammatory cytokines and adhesion molecules, including intercellular adhesion molecule-1 (ICAM-1), vascular cell adhesion molecule-1 (VCAM-1), and E-selectin, promoting immune cell recruitment. Our results demonstrated both Fresh- and Lyo-NVs significantly downregulated pro-inflammatory cytokine and adhesion molecule expression **(Figure 3B)**. Endothelial recovery was further evaluated via the cell migration assay. LPS treatment reduced hCAEC migration, whereas Fresh- and Lyo-NV treatment restored migration to levels not significantly different from the non-stimulated control (**Figure 3C**), indicating recovery toward baseline rather than enhancement beyond baseline. Additionally, immunofluorescence staining showed reduced VCAM-1 expression following MSC-NV treatment **(Figure 3D)**. Tube formation analysis demonstrated that MSC-NVs significantly restored endothelial angiogenic activity impaired by cyclosporin A (CyA) (**Figure 3E**). To assess angiogenic recovery, human umbilical vein endothelial cells (HUVECs) were cultured on Matrigel and co-treated with CyA and MSC-NVs 2 h after seeding. Quantitative analysis of junctions, master junctions, master segments, and total tube length confirmed that MSC-NV treatment restored tube formation impaired by CyA. The results indicated that MSC-NVs enhance angiogenic activity and endothelial function regardless of lyophilization.

Collectively, our findings suggested that MSC-NVs may offer a therapeutic advantage by simultaneously attenuating endothelial inflammatory signaling and promoting re-endothelialization under restenotic conditions. These effects are relevant given the limitations of conventional DESs, which suppress VSMC proliferation and may also impair endothelial recovery. Both Fresh- and Lyo-NVs retained anti-inflammatory and endothelial restorative effects, indicating that lyophilization does not compromise MSC-NV bioactivity. Conversely, quantitative real-time PCR (qRT-PCR) results showed greater suppression of *TNF*, *IL6*, *ICAM1*, *VCAM1*, and *SELE* expression in Lyo-NVs compared with Fresh-NVs. The enhanced suppression of selected inflammatory and endothelial dysfunction markers by Lyo-NVs suggested that lyophilization may modulate the relative abundance of specific regulatory miRNAs, although further mechanistic validation is required.

In vitro suppression of smooth muscle cell and adventitial fibroblast activation by MSC-NVs

The anti-inflammatory effects of MSC-NVs on human aortic smooth muscle cells (hAoSMCs) were evaluated under TNF-α (10 ng/mL) and interferon-γ (IFN-γ) (10 ng/mL) stimulation. Based on dose-dependent assessments of inflammatory regulation, metabolic activity, and cytotoxicity, 10 μg/mL (1.70×10^9 particles/mL) was selected for subsequent *in vitro* experiments. In hAoSMCs, Fresh- and Lyo-NVs generally attenuated TNF-α/IFN-γ-induced inflammatory marker expression across concentrations of 0.1–50 μg/mL, with robust effects at 10 μg/mL and limited or variable additional benefit at 50 μg/mL. CCK-8 analysis further showed attenuation of PDGF-BB-induced metabolic activity, while NV-only Live/Dead imaging showed no overt cytotoxicity up to 50 μg/mL **(Figure S4)**. No significant difference in uptake efficiency was observed between Fresh- and Lyo-NVs, consistent with our findings in ECs **(Figure 4A)**. A bilayered organ-on-a-chip system was used to assess transmural transport of MSC-NVs from the intima layer to the media layer, showing MSC-NVs were internalized in ECs and subsequently transported across the endothelial barrier and detected in SMCs (**Figure 4B**). Under inflammatory induction, *TNF*, *IL1B*, and *IL6* expression significantly increased in hAoSMCs **(Figure 4C)**. Fresh-NVs marginally attenuated *IL6* expression, whereas *TNF* and *IL1B* expression did not significantly change. In contrast, Lyo-NVs suppressed the expression of pro-inflammatory cytokines, including *TNF*, *IL1B*, and *IL6*.

Next, platelet-derived growth factor-BB (PDGF-BB), a key biomolecule for phenotypic switching of SMCs from a contractile to a synthetic phenotype, was combined with TNF-α and IFN-γ to mimic the restenotic microenvironment associated with neointimal hyperplasia [39-41]. Combined stimulation decreased *ACTA2*, *CNN1*, and *TAGLN* expression and increased *PDGFRB* expression. Fresh- and Lyo-NV treatment partially restored the contractile-marker profile and reduced *PDGFRB* expression **(Figure 4D)**. Under the same combined-stimulation condition, both Fresh- and Lyo-NVs reduced hAoSMC migration **(Figure 4E)** and partially restored α-SMA fiber anisotropy **(Figure 4F)**, supporting attenuation of SMC phenotypic switching.

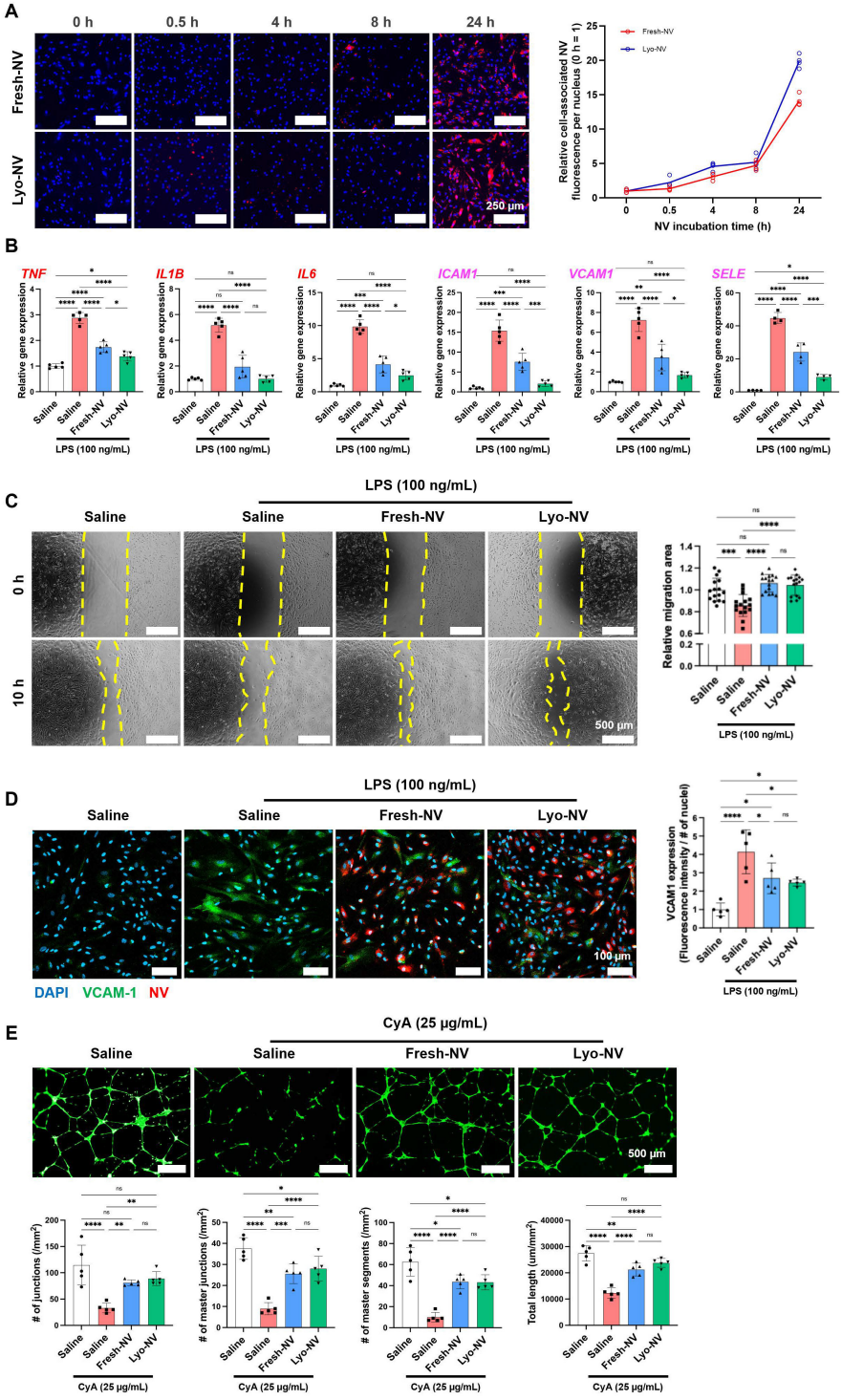


Figure 3. *In vitro* re-endothelialization and endothelial protective effects of MSC-NVs. (A) Time-dependent uptake of DiD-labeled Fresh- and Lyo-NVs in hCAECs was evaluated at 0, 0.5, 4, 8, and 24 h. Representative fluorescence images show DiD-labeled MSC-NVs (red) and DAPI-stained nuclei (blue). Cell-associated DiD fluorescence was quantified

per nucleus and normalized to the mean fluorescence value at 0 h (0 h = 1) (n = 4). Individual values and mean lines are shown. Scale bar = 250 μm. (B) Relative mRNA expression of pro-inflammatory and endothelial dysfunction markers in hCAECs determined via qRT-PCR (n = 4–5). (C) Representative images of a scratch assay performed on hCAECs following MSC-NV treatment at 0 and 10 h, with quantification of relative migration area at 10 h (n = 6). Values were normalized to the non-stimulated Saline control. Scale bar = 500 μm. (D) VCAM-1 expression (green) in hCAECs was determined via immunostaining quantification; nuclei were stained with 4′,6-diamidino-2-phenylindole (DAPI, blue) (n = 5). Scale bar = 100 μm. (E) Endothelial protective effects of MSC-NVs on CyA-impaired tube formation. Images and their quantification results show the vascular protective effect of MSC-NV treatment (n = 5). Scale bar = 500 μm. In panels B–D, the first Saline group represents the non-stimulated vehicle control. The horizontal bar labeled "LPS (100 ng/mL)" identifies the second Saline and MSC-NV-treated groups as LPS-stimulated; accordingly, the second Saline group represents the LPS-stimulated vehicle control. In panel E, the horizontal bar labeled "CyA" identifies the CyA-treated groups. Individual values and mean lines are shown in panel A. Quantitative data in panels B–E are expressed as mean ± SD. Comparisons among more than two groups were performed using one-way ANOVA followed by Tukey's multiple comparisons test. ns = non-significant, *$p < 0.05$, **$p < 0.01$, ***$p < 0.001$, ****$p < 0.0001$.

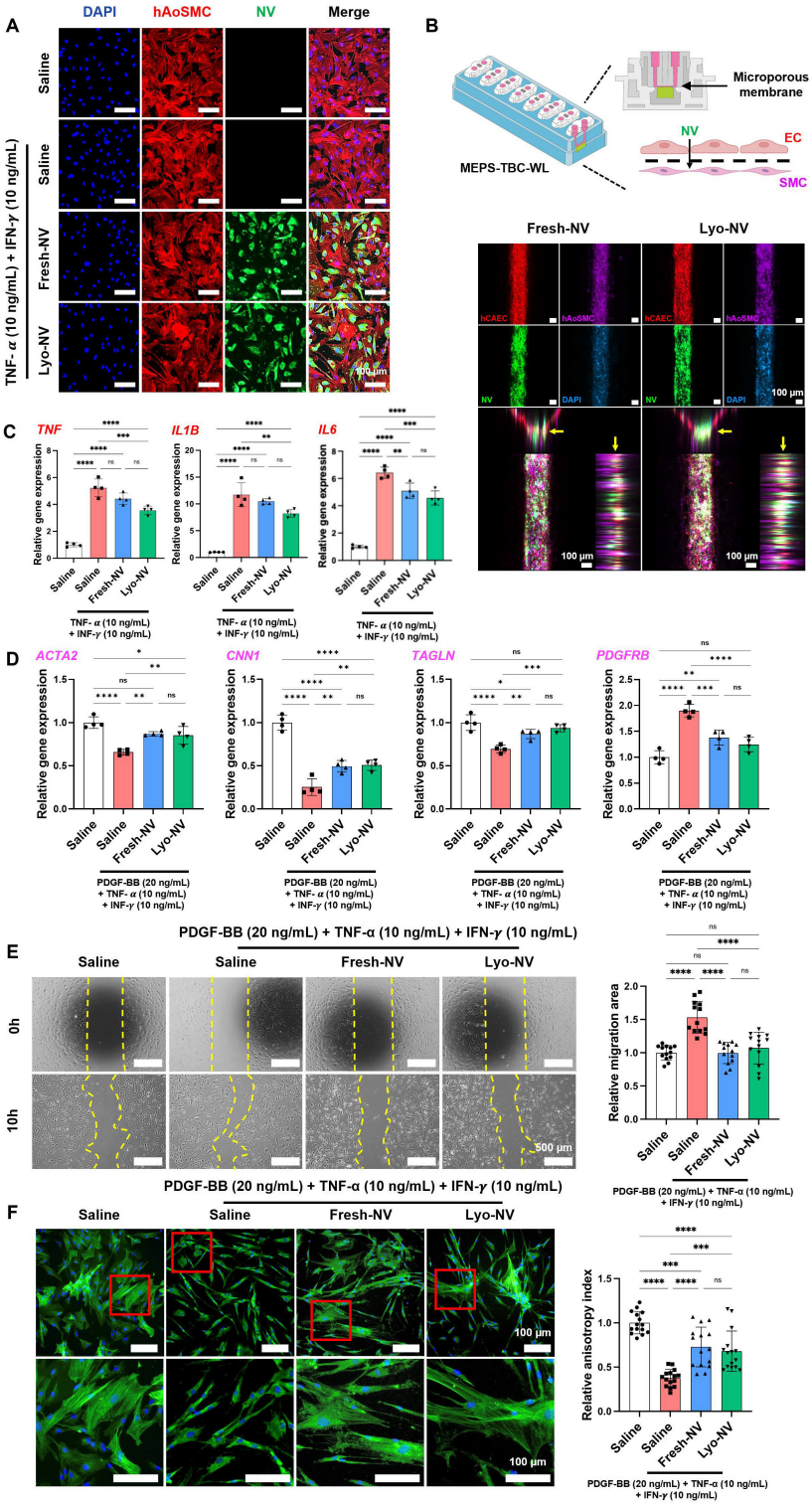


Figure 4. *In vitro* inhibition of smooth muscle cell activation via MSC-NVs. (A) MSC-NV internalization into hAoSMCs was visualized using F-actin (red) and DiO (green). Scale bar = 100 μm. (B) Representative images and schematic illustration of the organ-on-a-chip and cellular arrangement. Red indicates hCAECs, magenta hAoSMCs, and green NVs.

Yellow arrows indicate the porous membrane. Scale bar = 100 μm. (C) mRNA expression of pro-inflammatory markers in hAoSMCs determined via qRT-PCR (n = 4). (D) mRNA expression of hAoSMCs phenotype-associated markers *ACTA2*, *CNN1*, *TAGLN*, and *PDGFRB* under combined PDGF-BB, TNF-α, and IFN-γ stimulation, determined via qRT-PCR (n = 4). (E) Representative images of a scratch assay performed on hAoSMCs following MSC-NV treatment at 0 and 10 h time points under combined PDGF-BB, TNF-α, and IFN-γ stimulation, with quantification of the relative migration area (n = 5). Scale bar = 500 μm. (F) α-SMA fiber organization (green) in hAoSMCs under the same combined-stimulation condition was evaluated via immunostaining and quantified using the relative anisotropy index (blue: nucleus with DAPI staining) (n = 5). The lower panels show magnified views of the boxed regions. Scale bar = 100 μm. The first Saline group in panels C–F represents the non-stimulated vehicle control. The horizontal bars indicate TNF-α and IFN-γ stimulation in panel C and combined PDGF-BB, TNF-α, and IFN-γ stimulation in panels D–F; the second Saline group represents the corresponding stimulated vehicle control. Quantitative data are expressed as the mean ± SD. Comparisons among more than two groups were performed using one-way ANOVA followed by Tukey's multiple comparisons test. ns = non-significant, $^{**}p < 0.01$, $^{***}p < 0.001$, $^{****}p < 0.0001$.

These findings demonstrated that MSC-NVs retain the ability to regulate hAoSMC responses under inflammatory conditions relevant to vascular injury. In addition, the organ-on-a-chip system demonstrated transmural transport of MSC-NVs to the underlying SMC layer, indicating that MSC-NVs can affect both the intima and media layers. Furthermore, the combined stimulation model showed that MSC-NVs concurrently regulated transcriptional, migratory, and cytoskeletal features of SMC phenotypic modulation. The partial restoration of contractile-marker expression, reduction of *PDGFRB* expression and hAoSMC migration, and recovery of α-SMA fiber anisotropy suggested maintenance of a more contractile and homeostatic phenotype. As excessive SMC proliferation and transition to a synthetic phenotype drive neointimal hyperplasia and restenosis, these effects may be particularly relevant for vascular device applications.

Adventitial fibroblasts have been reported to contribute to neointimal formation and extracellular matrix remodeling following vascular injury [42, 43]. Therefore, the effects of MSC-NVs were additionally evaluated in TGF-β1-stimulated human vascular adventitial fibroblasts (hBVAFs). TGF-β1 treatment increased the α-SMA-positive area per nucleus and the expression of *ACTA2*, *TAGLN*, *POSTN*, and *COL3A1*. Fresh- and Lyo-NV treatment attenuated these changes, supporting suppression of myofibroblast activation and profibrotic remodeling **(Figure S5)**. Because fibroblast proliferation, migration, and accumulation were not directly evaluated, these findings were interpreted specifically as modulation of fibroblast activation.

Overall, these results suggested that MSC-NVs exert coordinated therapeutic effects on SMCs and adventitial fibroblasts by attenuating inflammation, SMC phenotypic activation, and profibrotic remodeling, thereby contributing to neointimal hyperplasia inhibition following stent implantation. Notably, these effects are comparable to those of conventional mTOR inhibitors, which primarily inhibit SMC proliferation and migration. In this context, the findings also address previous concerns that MSC-based therapies may promote SMC proliferation [44, 45]. Notably, the restoration of endothelial migration and angiogenic activity, together with the suppression of SMC and fibroblast activation, indicates coordinated regulation of vascular cell responses. This functional selectivity represents a key advantage of MSC-NVs, highlighting their potential as a vasculomodulatory therapy capable of simultaneously promoting endothelial recovery and preventing restenosis.

In vitro suppression of pro-atherogenic macrophage responses via MSC-NVs

Macrophages contribute to atherosclerosis by mediating vascular inflammation, differentiating into foam cells via oxidized low-density lipoprotein (ox-LDL) uptake, and driving foreign body responses that promote in-stent restenosis. To evaluate the anti-inflammatory effects of MSC-NVs on macrophages in vascular inflammation, THP-1-derived macrophages (THP-1Øs) were stimulated with LPS and IFN-γ to induce a pro-inflammatory phenotype. Both Fresh- and Lyo-NVs were efficiently internalized by THP-1Øs **(Figure 5A)**. Consistent with our previous findings, MSC-NV treatment suppressed the LPS- and IFN-γ-induced upregulation of *TNF*, *IL1B*, and *IL6* mRNA expression regardless of lyophilization **(Figure 5B)** [26]. Lyo-NVs were also associated with a modest increase in *IL13*, suggesting partial alleviation of inflammatory macrophage activation. In addition, both Fresh- and Lyo-NVs reduced inducible nitric oxide synthase (iNOS) expression in macrophages, as confirmed by immunofluorescence staining **(Figure 5C)**. Moreover, both Fresh- and Lyo-NVs significantly attenuated ox-LDL uptake in macrophages, indicating that MSC-NVs may inhibit further foam cell formation **(Figure 5D)**.

Collectively, these findings indicated that MSC-NVs effectively suppress pro-inflammatory macrophage activation in microenvironments mimicking post-stent implantation. Activated macrophages amplify local inflammation via sustained cytokine release and inflammatory signaling, aggravating endothelial injury and promoting VSMC activation [46, 47]. MSC-NVs attenuated pro-inflammatory macrophage responses and cytokine secretion while inhibiting foam cell formation. These effects highlight their therapeutic relevance in vascular interventions and their potential to modulate upstream atherogenic processes.

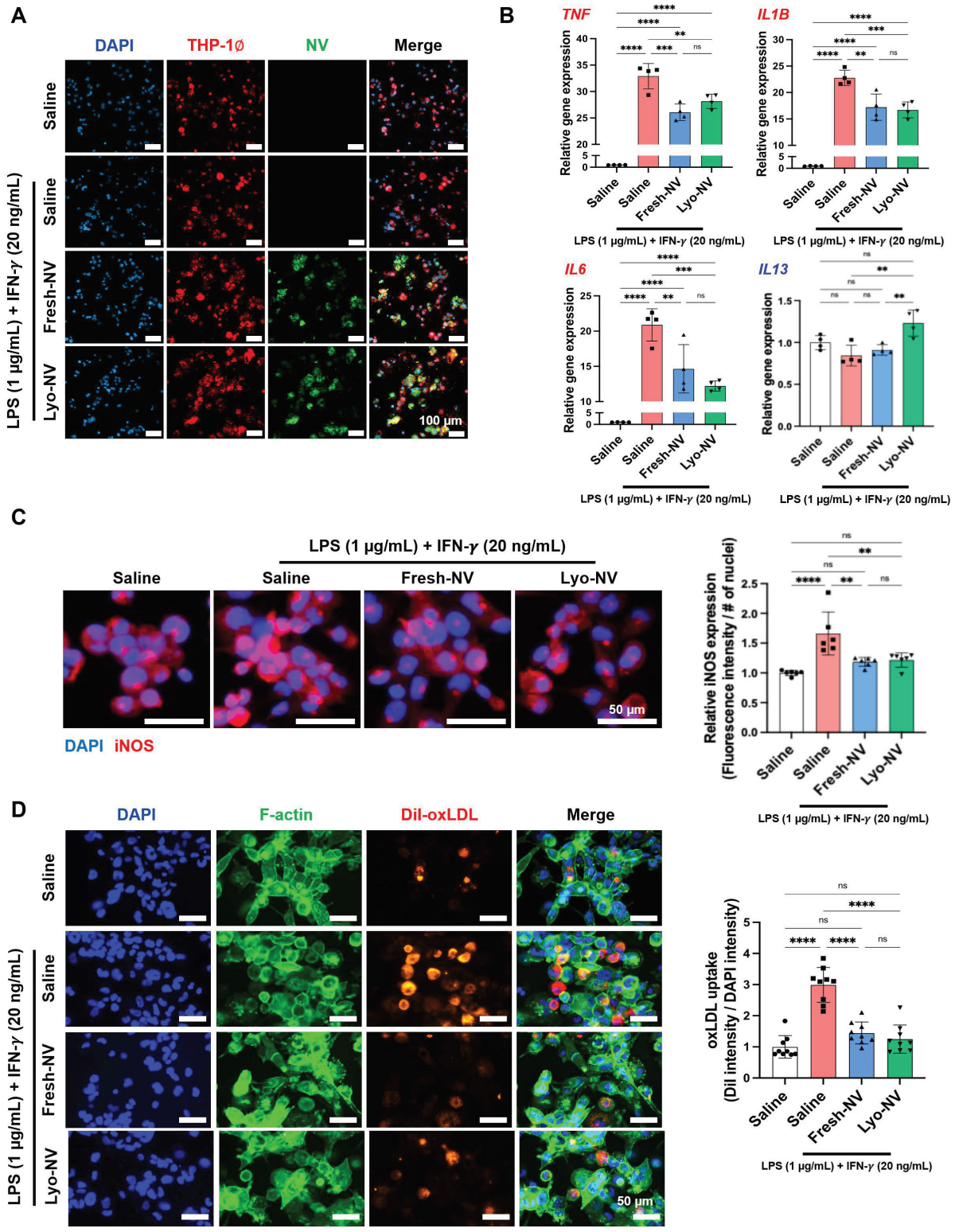


Figure 5. *In vitro* suppression of pro-atherogenic macrophage responses via MSC-NVs. (A) MSC-NVs internalization into THP-1 macrophages visualized using 1,1′-dioctadecyl-3,3,3′,3′-tetramethylindodicarbocyanine (DiD, red) and DiO (green). Scale bar = 100 μm. (B) mRNA expression of pro-inflammatory markers in THP-1 macrophages determined via qRT-PCR (n = 4). (C) iNOS expression (red) in THP-1 macrophages determined via immunostaining quantification (blue: nucleus with DAPI staining) (n = 6). Scale bar = 50 μm. (D) DiI-labeled ox-LDL (DiI-ox-LDL) uptake assay in THP-1 macrophages treated with LPS and IFN-γ (n = 9). Scale bar = 50 μm. Quantitative data are expressed as the mean ± SD. Comparisons among more than two groups were performed using one-way ANOVA followed by Tukey's multiple comparisons test. ns = non-significant, $^{**}p < 0.01$, $^{***}p < 0.001$, $^{****}p < 0.0001$.

Procedural outcomes, follow-up angiography, and optical coherence tomography findings

Successful establishment of the restenosis rabbit model before BRS implantation was confirmed by angiography, optical coherence tomography (OCT), and histological analyses **(Figure S6)**. Angiographic analysis demonstrated that the mean luminal diameter in the balloon injury artery was significantly decreased compared with that in the normal artery at 1 week after balloon injury (1.47 ± 0.39 mm vs. 2.43 ± 0.17 mm; $p < 0.001$, two-sample t-test). OCT analysis also confirmed a significantly smaller lumen area in the balloon injury artery than in the normal artery (1.45 ± 0.05 mm^2 vs. 4.01 ± 0.17 mm^2; $p < 0.001$, two-sample t-test). Histological evaluation using hematoxylin and eosin (H&E) staining demonstrated a significant increase in the thickness of intimal tissue in balloon injury artery compared with the normal artery (0.43 ± 0.11 mm vs. 0.18 ± 0.03 mm; $p < 0.001$, two-sample t-test). These findings confirm that balloon injury successfully induced reproducible luminal narrowing and neointimal hyperplasia, thereby establishing a restenotic vascular environment that more closely reflects the pathological conditions. The use of this pre-existing restenosis model provides a more stringent and clinically relevant platform for evaluating the therapeutic performance of NVE-BRS, particularly its effects on vascular healing, neointimal remodeling, and prevention of recurrent restenosis.

Angiographic and OCT analyses evaluated vascular patency and neointimal hyperplasia following NVE-BRS implantation. BRS placement was successful in all study groups. All rabbits survived to the end of the study without procedure-related complications. Follow-up angiography and OCT findings are shown in **Figure 6A** and summarized in **Table S1**. Follow-up angiography at 4 weeks revealed maintained BRS patency after the BRS placement in both the bare BRS and NVE-BRS groups **(Figure 6B)**. Additionally, reduced neointimal formation was observed in the NVE-BRS group compared with the bare BRS group, as assessed via OCT analysis **(Figure 6C)**. The luminal diameter change, reflecting late lumen loss, was significantly lower in the NVE-BRS group than in the bare BRS group **(Figure 6D)**, whereas the actual luminal diameter was significantly higher in the NVE-BRS group, indicating better preservation of vessel patency (all $p < 0.01$, two-sample t-test) **(Figure 6E)**. Neointimal thickness at stented arteries was significantly lower in the NVE-BRS group than that in the bare BRS group (0.17 mm ± 0.01 vs. 0.40 mm ± 0.02; $p < 0.001$, two-sample t-test) **(Figure 6F)**. Furthermore, the percentage of stenosis area (SA) was also significantly lower in the NVE-BRS group than in the bare BRS group (19.38% ± 1.67 vs. 48.8% ± 1.56; $p < 0.001$, two-sample t-test) **(Figure 6G)**. Angiography and OCT findings demonstrated that NVE-BRS suppressed inflammatory tissue responses and severe neointimal tissue formation caused by BRS-induced mechanical injury in the balloon-injured rabbit iliac artery. In contrast, the bare BRS used in this study primarily provided only transient mechanical support and relied on passive vascular healing. This passive response resulted in heterogeneous endothelial coverage and excessive SMC proliferation, contributing to BRS restenosis [48, 49]. MSC-NV has potentials to inhibit SMC proliferation and promote an anti-inflammatory effect [50]. NVE-BRS enables localized MSC-NV delivery to the target artery, actively modulating the vascular tissue response microenvironment. Exosome eluting stents promote endothelial migration and coverage while suppressing excessive neointimal formation via paracrine signaling rather than cytotoxic inhibition [30]. Consistent with this mechanism, steadily released MSC-NVs actively promote regulated endothelial and SMC responses from the initial inflammatory phase to late vascular remodeling. Our results demonstrated that direct and localized delivery of MSC-NVs via BRS effectively suppress excessive neointimal tissue formation after BRS placement in the balloon-injured rabbit iliac artery. NVE-BRS demonstrates therapeutic potential for restenosis prevention while offering biocompatibility and eliminating the need for BRS removal. As a preliminary tissue-level safety assessment, representative H&E-stained sections of the heart, liver, lung, and kidney showed no overt histopathological abnormalities in either the bare BRS or NVE-BRS group at 4 weeks **(Figure S7)**.

The present study was designed to evaluate the early biological response following NVE-BRS implantation using a balloon-injured rabbit iliac artery model rather than long-term scaffold degradation. This model provides a reproducible and well-established platform for assessing vascular remodeling and restenosis after BRS implantation, although it does not fully recapitulate human atherosclerotic coronary disease. Vascular healing after BRS implantation progresses through overlapping phases involving acute thrombosis and inflammation, SMC migration, extracellular matrix deposition, re-endothelialization, and subsequent neointimal maturation [51, 52]. In rabbits, these processes occur more rapidly than in humans, with a substantial neointimal response generally established within 28 days [53]. Accordingly, the 4-week endpoint captures the transition from the active proliferative phase to early vascular remodeling and enables assessment of scaffold patency, luminal stenosis,

neointimal formation, endothelial recovery, fibrin deposition, inflammatory responses, and vascular injury [52, 54]. Although PLLA-based BRSs require approximately 2–3 years for complete bioresorption, the present findings should therefore be interpreted as evidence of early vasculomodulatory effects rather than long-term scaffold performance. Future studies should extend validation to atherosclerotic disease models and larger-animal coronary models, particularly porcine systems, to evaluate NVE-BRS under more clinically relevant vascular anatomy, plaque burden, and healing conditions while incorporating cardiac functional assessment as part of a comprehensive cardiovascular safety evaluation.

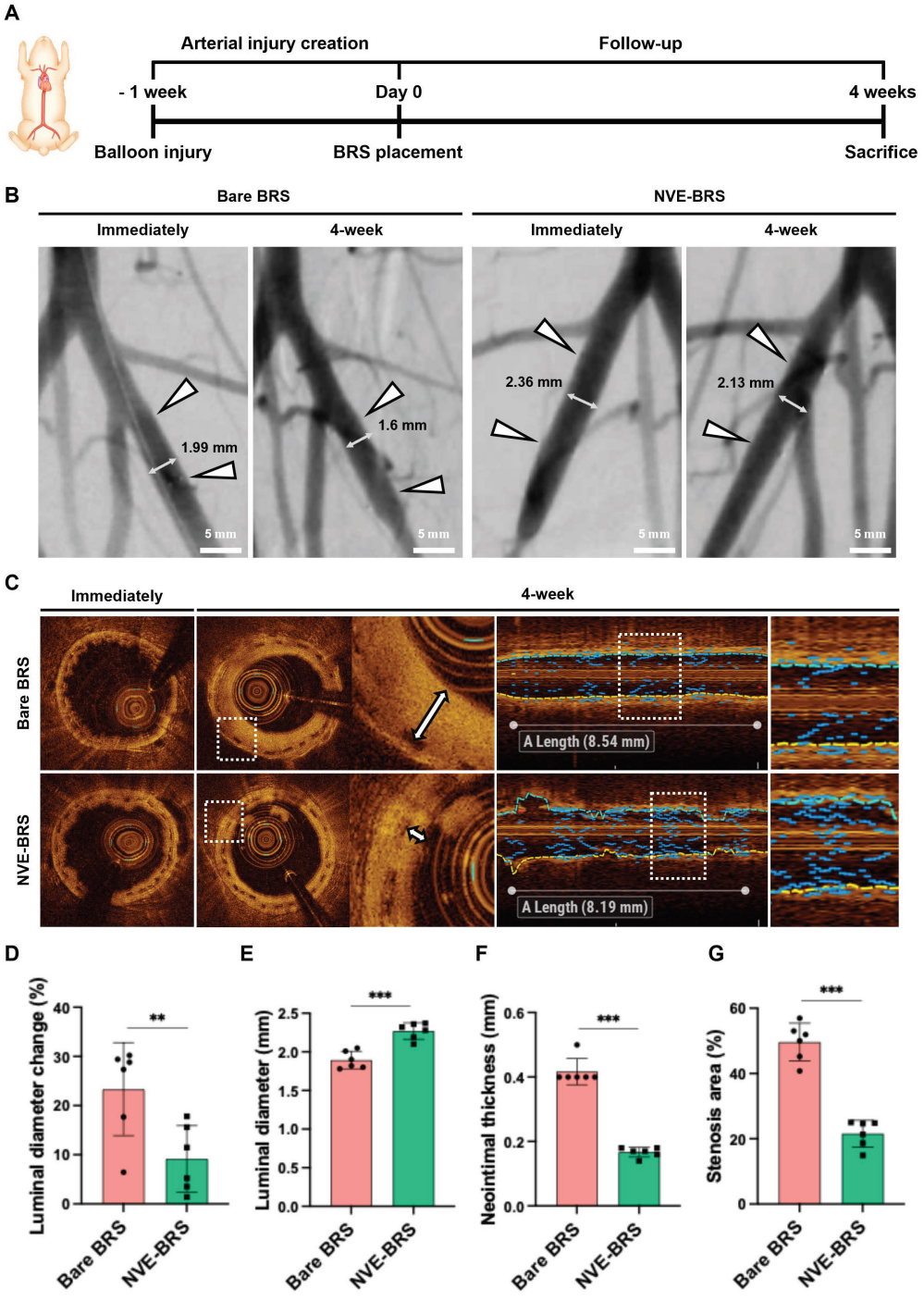


Figure 6. Follow-up angiography and optical coherence tomography (OCT) findings after BRS placement in a balloon-injured rabbit iliac artery model. (A) Flow diagram of the study design and follow-up. (B) Representative angiography images obtained before, immediately after, and 4 weeks after BRS placement show BRS patency (arrowhead) (white double-headed arrows, OCT analysis segments) in the study groups. (C) OCT images obtained immediately and at 4 weeks after BRS placement show the extent of neointimal tissue formation (white double-headed arrows) in the bare BRS and NVE-BRS groups. (D) Graphs show the percentage of luminal diameter change obtained via follow-up angiography, (E) mean luminal diameter, (F) mean neointimal thickness, and (G) percentage of stenosis area obtained from follow-up OCT at 4 weeks after BRS placement. Data are expressed as the mean ± SD. $^{**}p < 0.01$, $^{***}p < 0.001$.

Coordinated vasculomodulation by NVE-BRS

Histological and immunofluorescence analyses assessed vascular remodeling, including inflammation, neointimal formation, and re-endothelialization, following NVE-BRS implantation. Quantitative results are summarized in **Table S1**, and the representative H&E and MT staining images are provided in **Figure S8**. First, at 28 days after implantation, DiD-associated MSC-NV fluorescence remained detectable along the NVE-BRS struts and within deeper regions of the vascular wall **(Figure 7A)**. Hematoxylin and eosin (H&E) staining showed that inflammatory cell infiltration was significantly lower in the NVE-BRS group than in the bare BRS group ($p < 0.001$, Mann–Whitney U test) **(Figure 7B)**. Masson's trichrome (MT) staining showed that fibrin **(Figure 7C)** and collagen deposition **(Figure 7D)** were significantly reduced in the NVE-BRS group compared with the bare BRS group (all $p < 0.001$, Mann–Whitney U test). Verhoeff-Van Gieson (VVG) staining further demonstrated elastic lamina (EL) structure preservation in the NVE-BRS group; however, it was disrupted in the bare BRS group ($p < 0.001$, Mann–Whitney U test) **(Figure 7E)**. Representative low-magnification images of the entire vessel cross-sections are provided in **Figure S9.** Immunofluorescence staining further showed that VCAM-1- **(Figure 7H)**, platelet-derived growth factor receptor-β (PDGFR-β)- **(Figure 7I)**, α-SMA- **(Figure 7J)**, and CD68-positive areas **(Figure 7K)** were significantly reduced in the NVE-BRS group, and CD31-positive endothelial coverage was significantly higher than in the bare BRS group ($p < 0.001$, Mann–Whitney U test) **(Figure 7G)**, indicating suppressed SMC activation and macrophage infiltration, and enhanced EC recruitment in the NVE-BRS group. In conventional BRS implants, neointimal tissue thickness ranged from 0.35 to 0.50 mm at 28–30 d. This neointima showed severe collagen deposition and increased inflammatory cell infiltration, comprising approximately 50–60% of the neointimal area [55, 56].

Conventional antiproliferative drug-coated BRS have been extensively investigated for restenosis prevention through sustained release of agents such as sirolimus (SRL) and everolimus. While these platforms effectively suppress neointimal hyperplasia, previous studies have also reported delayed endothelial recovery resulting from the non-selective antiproliferative effects of these agents [57]. Additional comparison with sirolimus-eluting bioresorbable scaffold (SRL-BRS) further supported the role of NVE-BRS in therapeutic decoupling of neointimal suppression and re-endothelialization. NVE-BRS showed significantly lower tunica intima thickness, higher CD31-positive deposition, and lower α-SMA-positive deposition than both bare BRS and SRL-BRS (all $p < 0.001$) **(Figure S10).**

The increased CD31-positive endothelial coverage in the NVE-BRS group suggested accelerated and stabilized re-endothelialization. ECs were aligned between the implanted BRS and lumen, indicating formation of a continuous endothelial layer covering the BRS surface. This endothelial coverage may enhance barrier integrity and reduce platelet adhesion and inflammatory cell infiltration, suppressing late-stage thrombosis and restenosis [58, 59]. These findings are consistent with the *in vitro* results shown in **Figure 3**, demonstrating enhanced endothelial migration and tube formation. Together, these results support a mechanistic link between MSC-NV treatment and improved endothelial recovery and tubular network formation. The *in vivo* findings also supported that NVE-BRS significantly inhibits inflammatory cell infiltration and fibrotic tissue remodeling via the local MSC-NV release. Together with the computational analysis in **Figure 2** showing predicted outward diffusion and local retention of the MSC-NVs within the arterial wall, and the organ-on-a-chip model in **Figure 4B** demonstrating their transendothelial migration, the persistent DiD-associated signal at 28 days supports local MSC-NV distribution across the intimal and medial vascular compartments. In addition, the preservation of EL integrity in the NVE-BRS group suggested attenuation of pathological vascular remodeling as EL fragmentation is a consistent early adverse finding in polymeric BRSs and is closely associated with exaggerated neointimal proliferation [9, 55]. Reduced PDGFR-β- and α-SMA-positive deposition near the BRS in the NVE-BRS group was consistent with the *in vitro* findings in **Figure 4**, demonstrating inhibition of SMC activation via MSC-NVs and supporting a mechanistic basis for neointimal hyperplasia suppression. Inflammatory responses after BRS implantation were attenuated in the NVE-BRS group, as evidenced by reduced VCAM-1 expression, indicating decreased monocyte recruitment, and decreased CD68-positive macrophage infiltration. These findings are consistent with the *in vitro* results shown in **Figures 3** and **Figure 5**. The reduced collagen deposition observed in the NVE-BRS group may also partly reflect attenuation of profibrotic remodeling, consistent with the *in vitro* hBVAF findings in **Figure S5**. In contrast, the bare BRS group showed persistent VCAM-1 upregulation and CD68-positive areas reaching 20–25% during early vascular healing, reflecting a pro-inflammatory microenvironment consistent with previous studies [60]. Overall, MSC-NVs released from NVE-BRS modulate the early

inflammatory phase, facilitate endothelial recovery during healing, and suppress the late proliferative phase following BRS placement, providing temporally coordinated regulation of vascular remodeling.

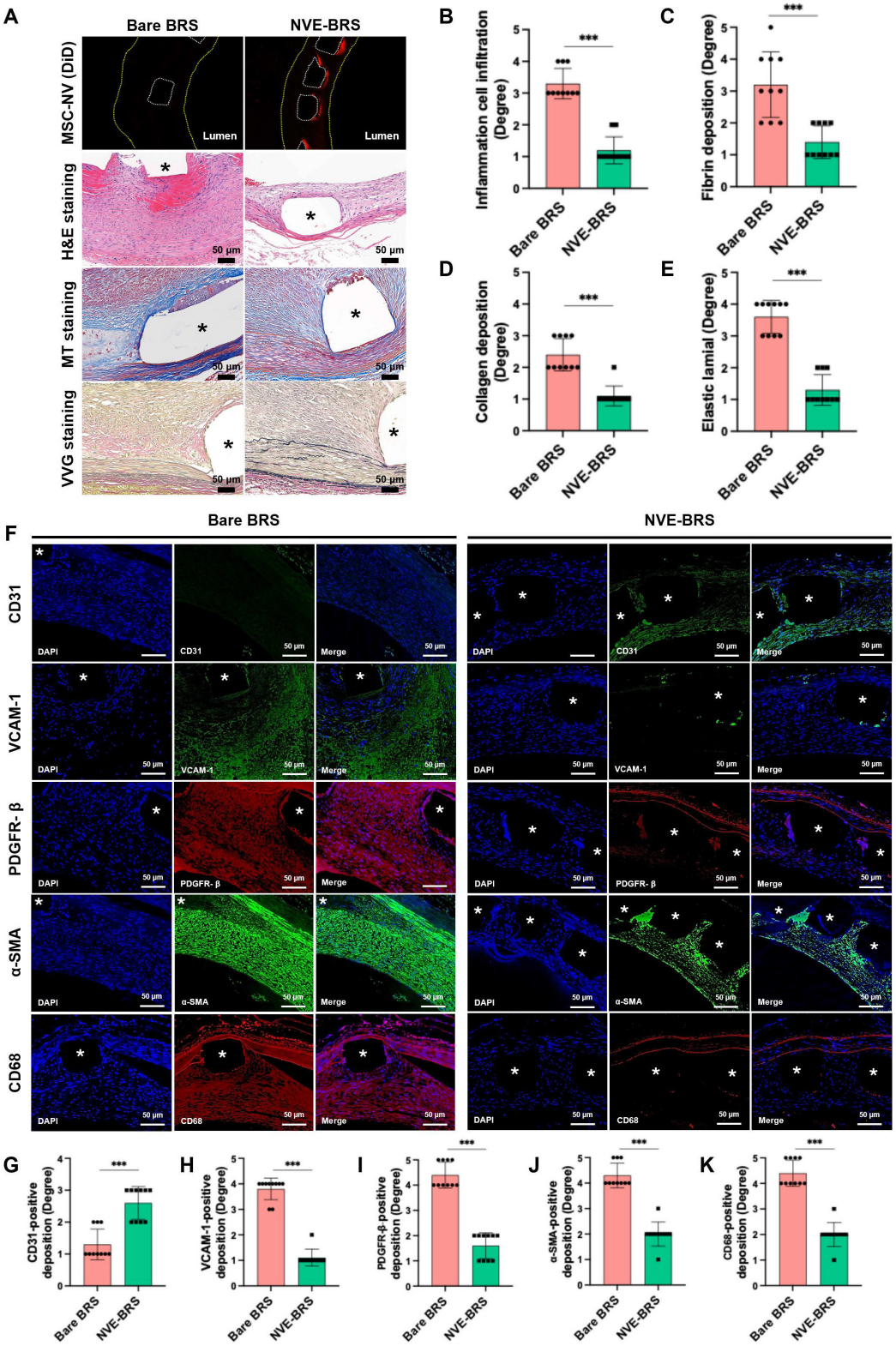


Figure 7. Representative microscopic and immunofluorescence images of histological sections in the bare BRS and NVE-BRS groups. (A) Distribution of DiD-stained MSC-NVs and histological staining with H&E, MT, and VVG in the bare BRS and NVE-BRS groups (star, BRS strut). Graphs show the mean degrees of (B) inflammatory cell infiltration, (C) fibrin deposition, (D) collagen deposition, and (E) EL changes with statistical comparisons in between study groups. (F) CD31, VCAM-1, PDGFR-β, α-SMA, and CD68 immunofluorescence images show significant differences between study groups (star, BRS strut). Graphs show mean degrees of positive deposition of (G) CD31, (H) VCAM-1, (I) PDGFR-β, (J) α-SMA, and (K) CD68 with statistical analysis for each group. Star = scaffold strut. Data are expressed as the mean ± SD. ***$p < 0.001$.

Despite its strong therapeutic efficacy, biocompatibility, and off-the-shelf potential enabled by lyophilized MSC-NVs, additional manufacturing and quality-control requirements must be addressed before clinical translation of NVE-BRS. First, reproducible MSC-NV manufacturing will require control of MSC source and culture conditions, extrusion yield, vesicle size and number, molecular cargo, surface-marker profile, and functional potency to ensure batch-to-batch consistency. Previous demonstrations of reproducible GMP manufacturing of extrusion-derived cell vesicles support the feasibility of standardized MSC-NV production [61], while current EV characterization frameworks may provide a basis for defining vesicle-related quality attributes [62]. Second, the long-term stability of the assembled NVE-BRS product must be established beyond the short-term preservation of lyophilized MSC-NVs demonstrated in the present study. This should include retention of NV bioactivity, coating integrity, and scaffold mechanical properties after prolonged storage, crimping, and deployment. Trehalose-assisted lyophilization may support off-the-shelf storage of stem-cell-derived vesicles [27]; however, the shelf life and retained performance of the final NVE-BRS product remain to be determined. Sterilization compatibility should also be considered, preferably by sterilizing the scaffold components before MSC-NV loading, followed by aseptic NV coating and final assembly under GMP-compliant conditions to preserve MSC-NV bioactivity and coating integrity. Finally, batch-release criteria for NVE-BRS should integrate vesicle-level and scaffold-level attributes, including NV loading per scaffold, coating coverage and uniformity, release profile, retained biological potency, and post-deployment mechanical integrity.

MSC-NV miRNA cargo associated with coordinated vasculomodulation

The vasculomodulatory effects described above were observed across ECs, SMCs, adventitial fibroblasts, and macrophages. To further investigate the MSC-NV components associated with these effects, the miRNA cargo of MSC-NVs was analyzed via small RNA sequencing, which showed consistent expression profiles across replicates (**Table S2**). The 50 most abundant miRNAs included several members of the let-7 family, together with miR-21-5p, miR-100-5p, miR-221-3p, miR-199a-3p, miR-10a-5p, and miR-143-3p **(Figure 8A)**. Retrieval of experimentally validated targets of the top 50 miRNAs yielded 1,024 unique genes from a background of 2,502 validated targets of all miRNAs detected in MSC-NVs (**Table S3**). Among 670 significantly enriched gene ontology (GO) biological process terms, 72 were classified into four vascular remodeling-related categories: endothelialization (30 terms), inflammation (19 terms), VSMC activation (13 terms), and fibroblast activation (10 terms) **(Figure 8C-F, Table S4)**. Among 421 target genes annotated to these terms, 55 genes targeted by four or more of the top 50 miRNAs were defined as hub genes. Through these hub genes, 38 of the top 50 miRNAs were connected to one or more of the four categories **(Figure 8B)**, and the corresponding miRNA-target-GO relationships are shown in **Figure S11**. These findings suggested that several highly abundant MSC-NV miRNAs are associated with common target genes involved in vascular remodeling.

In the endothelialization category, enriched GO terms included regulation of angiogenesis, blood vessel EC migration, and regulation of the EC apoptotic process **(Figure 8C, Table S5)**. Several abundant MSC-NV miRNAs have previously been associated with endothelial function. miR-21 has been reported to regulate PTEN-dependent endothelial signaling and miR-10a to limit pro-inflammatory NF-κB signaling in the endothelium, whereas miR-27b has been associated with endothelial sprouting and angiogenesis [63-65]. These reported functions were consistent with the reduced endothelial inflammatory responses, restored hCAEC migration, and recovery of angiogenic activity observed following MSC-NV treatment **(Figure 3B-E)**, suggesting that the miRNA cargo of MSC-NVs may partly contribute to endothelial recovery. In the VSMC activation category, enriched GO terms were mainly associated with SMC proliferation **(Figure 8D, Table S5)**, and the hub genes annotated to these terms included *KLF4*, *MYC*, and *CDK6* **(Figure 8B)**. miR-143 has been reported to regulate SMC phenotype through the *KLF4*-associated transcriptional network, and miR-24 and miR-29a to regulate PDGFR-β in the SMC response to vascular injury [66], while miR-22, miR-140-3p, and miR-23b-3p have been associated with suppression of SMC phenotypic modulation or neointimal hyperplasia [67-69]. These findings were consistent with the partial restoration of *ACTA2*, *CNN1*, and *TAGLN* expression, reduced *PDGFRB* expression and hAoSMC migration, and recovery of α-SMA fiber organization following MSC-NV treatment **(Figure 4D–F)**, suggesting that the MSC-NV miRNA cargo may contribute to maintenance of a more contractile and homeostatic SMC phenotype.

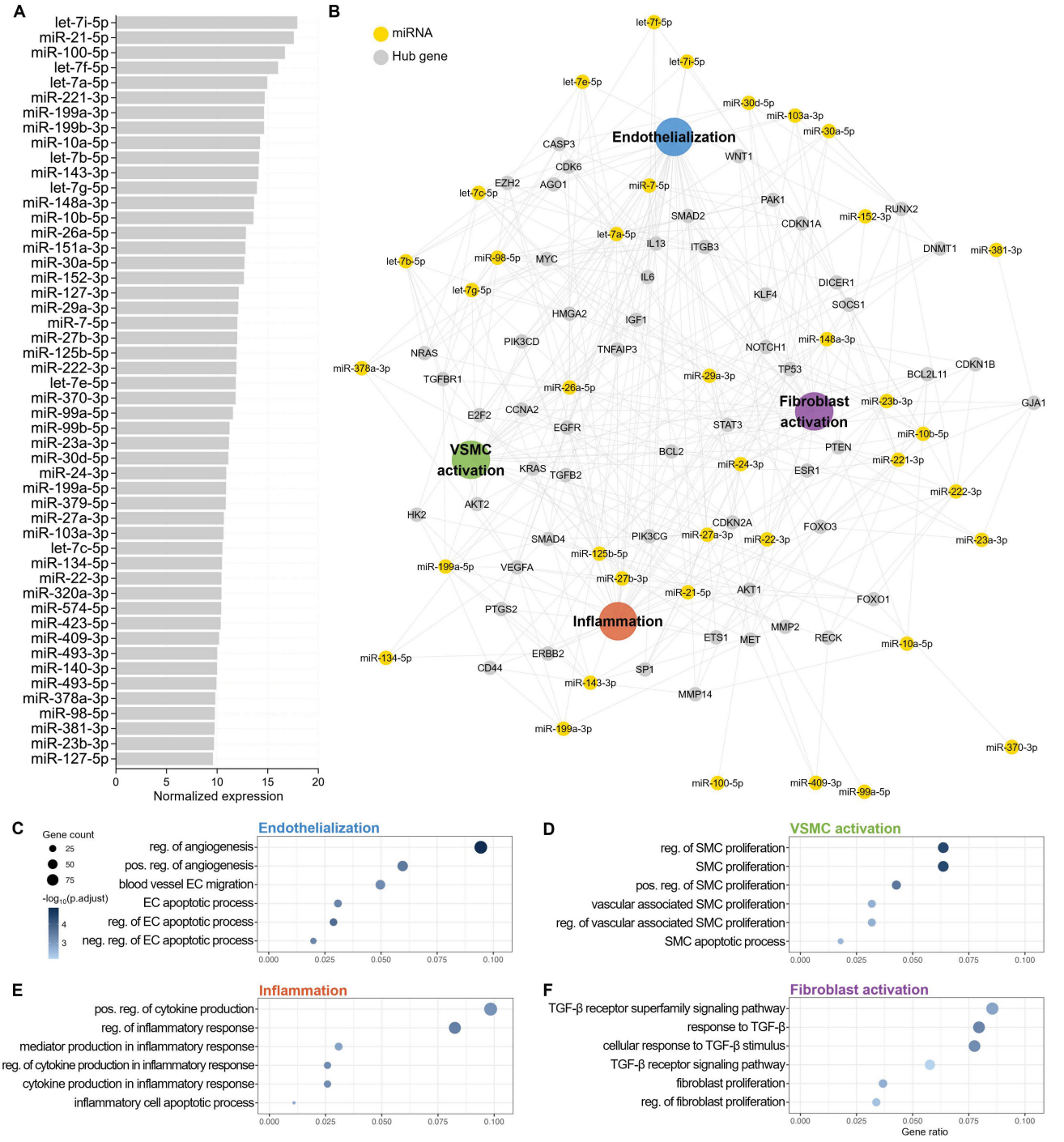


Figure 8. miRNA cargo of MSC-derived nanovesicles (MSC-NV) targets genes enriched in four vascular-remodeling-relevant processes. (A) Top 50 most abundant miRNAs in MSC-NV (n = 3), ranked by normalized expression (mean log2 TMM-CPM). (B) Network of the miRNAs in (A) (yellow), their target genes shared by ≥4 miRNAs ("Hub gene", grey), and the four mechanism categories (large colored nodes). (C-F) GO Biological Process terms enriched among validated targets of the miRNAs in (A), shown separately for each mechanism category: (C) Endothelialization, (D) VSMC activation, (E) Inflammation, and (F) Fibroblast activation.

In the fibroblast activation category, enriched GO terms were predominantly associated with TGF-β signaling **(Figure 8F, Table S5)**, and the hub genes annotated to these terms included *SMAD2*, *SMAD4*, and *TGFB2* **(Figure 8B)**. miR-27b has been reported to inhibit fibroblast activation through TGF-β signaling, and the miR-29 family to repress collagen and other extracellular matrix genes [70, 71], consistent with the reduced α-SMA-positive area per nucleus and the attenuated *ACTA2*, *TAGLN*, *POSTN*, and *COL3A1* expression observed in TGF-β1-stimulated hBVAFs following MSC-NV treatment **(Figure S5)**. Inflammation-related GO terms were associated with regulation of inflammatory responses and cytokine

production rather than with macrophage-specific processes **(Figure 8E, Table S5)**. However, let-7c has been reported to regulate macrophage polarization, and miR-22 to regulate macrophage polarization and *NLRP3* activation [72], which was consistent with the reduced inflammatory cytokine expression, iNOS expression, and ox-LDL uptake observed in THP-1-derived macrophages **(Figure 5B–D)**.

Collectively, these findings suggested that the miRNA cargo of MSC-NVs is associated with biological processes involved in endothelial recovery, VSMC phenotypic modulation, inflammatory regulation, and fibroblast activation, and may partly explain the coordinated vascular responses observed in this study. However, several limitations apply to this interpretation. GO enrichment does not indicate the direction of biological regulation, and the most abundant miRNAs included species with context-dependent or opposing reported activities in the same cell type. The analysis also describes the relative abundance of miRNAs within MSC-NVs rather than their enrichment relative to the parental cells, and individual miRNAs and their target genes were not experimentally validated in MSC-NV-treated cells. Further studies are therefore required to determine the specific contributions of individual miRNAs to these effects.

Conclusion

Current DESs primarily use antiproliferative agents to suppress VSMC proliferation, whereas this non-selective inhibition also impairs endothelial regeneration, contributing to restenosis and late thrombosis. This limitation highlights the need for a cell-dichotomous therapeutic strategy for synchronized vascular repair that selectively promotes re-endothelialization while suppressing pathological inflammation and VSMC activation, thereby enabling therapeutic decoupling between restenosis prevention and vascular healing. Accordingly, a vasculomodulatory engineering platform was developed that integrates MSC-NVs onto a BRS to enable balanced vascular healing while addressing key translational barriers. NVE-BRS was optimized with a thin-strut microarchitecture that facilitates efficient transmural MSC-NV diffusion into deep vascular tissue, while maintaining structural integrity and radial strength for effective scaffolding. MSC-NVs were integrated using a non-covalent surface modification strategy based on amphiphilic polymers. This approach preserves NV signaling cargo and native bioactivity by avoiding harsh chemical denaturation, while providing a highly biocompatible interface that minimizes the inflammatory response associated with complex chemical conjugation. Preservation of MSC-NV bioactivity following lyophilization highlights their suitability for long-term storage, manufacturing, and clinical deployment. Notably, this platform is inherently adaptable and could incorporate patient-derived MSC-NVs or various EV-related therapeutics in the future, supporting personalized and clinically scalable anti-restenotic therapies. Collectively, these findings position the NVE-BRS as a clinically translatable and highly effective alternative to conventional non-selective drug-based stent technologies, establishing a versatile platform for next-generation regenerative vascular implants.

Materials and Methods

Cell culture

Human adipose-derived stem cells (hASCs; PT-5006) and HUVECs (CC-2519) were purchased from Lonza (Basel, Switzerland). hCAECs (#6020), hAoSMCs (#6110), and hBVAFs (#1110) were purchased from ScienCell (Carlsbad, CA, USA). Human monocytic leukemia THP-1 cells (THP-1s; TIB-202) were purchased from ATCC (Manassas, VA, USA). hASCs, HUVECs, hCAECs, hAoSMCs, hBVAFs, and THP-1 cells were cultured in low-glucose Dulbecco's modified Eagle's medium (Thermo Fisher Scientific, Waltham, MA, USA), EGM® Endothelial Cell Growth Medium BulletKit® (CC-3124, Lonza), Endothelial Cell Medium (#1001, ScienCell), Smooth Muscle Cell Medium (#1101, ScienCell), Fibroblast Medium (# 2301, ScienCell), and RPMI-1640 medium (R8758, Sigma-Aldrich, St. Louis, MO, USA), respectively. All media were supplemented with 10% fetal bovine serum (FBS; Thermo Fisher Scientific) and 1% penicillin-streptomycin (P/S; Cytiva, Marlborough, MA, USA). Adherent cells were passaged at 80% confluency using 0.25% trypsin-EDTA (Thermo Fisher Scientific). THP-1 cells were treated with 200 nM phorbol 12-myristate 13-acetate (PMA; Sigma-Aldrich) for 24 h to induce macrophage-like differentiation. All experiments used cells between passages 3 and 6, except THP-1 cells.

MSC-NV preparation

For MSC-NV extrusion, MSCs reaching 80% confluency in 150 mm dishes were washed twice with Dulbecco's phosphate-buffered saline (DPBS; Welgene, Gyeongsan, Republic of Korea). Subsequently, cells were detached via incubation with 0.25% trypsin-EDTA solution for 3 min, and centrifuged at 200 × *g* for 3 min. The cell pellet was resuspended in DPBS. The cell suspension was serially extruded through polycarbonate membranes (Cytiva) with pore sizes of 10, 5, and 0.4 μm using a mini-

extruder kit (Avanti Polar Lipids Inc., Birmingham, AL, USA). For each membrane pore size, the suspension was extruded through the membrane six times. The solution extruded through the 0.4 μm membrane was washed three times by centrifugation at 21,400 × *g* for 30 min each. After washing, NVs were resuspended in fresh DPBS and quantified using a BCA protein assay kit (iNtRON Biotech, Seongnam, Republic of Korea). The isolated NVs were stored at −80 °C until further experiments.

NVE-BRS preparation and coating-concentration analysis

MSC-NVs were resuspended in a 4% trehalose solution at a protein-equivalent concentration of 700 μg/mL (1.19×10^{11} particles/mL). PMB30W-functionalized BRSs were coated with 100 μL of the MSC-NV suspension per scaffold, incubated for 10 min, and subsequently lyophilized.

To evaluate the effect of MSC-NV concentration on scaffold coating, DiD-labeled MSC-NVs were applied at 400, 700, or 1,000 μg/mL under otherwise identical coating conditions. Confocal fluorescence images were acquired using a confocal microscope (LSM800Airy, Carl Zeiss, Germany) under identical imaging parameters for all groups. The DiD-positive area was quantified using ImageJ (version 1.54g; National Institutes of Health) and expressed as the percentage of the scaffold area occupied by DiD fluorescence. Six independent scaffolds were analyzed per group.

Numerical simulation for NV diffusion

The transport of NVs from the BRS to the arterial wall was simulated using ANSYS Fluent 2023 R1. The computational domain was spatially discretized using a hybrid mesh consisting of 2.5 million mixed-cell elements [73]. NV transport was modeled by solving the transient advection-diffusion equation for concentration, *C*, within the arterial domain:

$$\frac{\partial \rho C}{\partial t} + \nabla \cdot (\rho \boldsymbol{u} C) = \nabla \cdot (D \nabla C)$$

where ρ denotes the domain density, u is the velocity vector, and *D* is the diffusion coefficient of the NVs. To account for physiological hemodynamics, blood viscosity ($\boldsymbol{\mu}$) within the lumen was modeled as a non-Newtonian fluid using the Carreau-Yasuda model [74]:

$$\mu = \mu_\infty + (\mu_0 - \mu_\infty)[1 + (\lambda\dot{\gamma})^2]^{\frac{n-1}{2}}$$

where μ_0 and μ_∞ are the zero-shear and infinite-shear viscosity limits, respectively, $\dot{\gamma}$ is the shear rate, and λ is the relaxation time. To simulate a physiological elution window of 28 days within a computationally feasible timeframe, a time-compression scaling factor of $S = 1000$ was applied, reducing the physical simulation duration to feasible time steps. The transient release of NVs from the BRS was described using an exponentially decaying mass flux to account for depletion of the carrier:

$$J(t) = J_0 exp\left(-\frac{t}{\tau_s}\right)$$

where J_0 is the initial mass flux, normalized to 1, and $\tau_s = 262.656$ s is the scaled decay constant. This value was derived under the assumption that the physical mass flux decreases to 1% of its initial maximum value over the 14-day elution window. To model physiological clearance by the perivascular system, a perfect-sink Dirichlet boundary condition ($C = 0$) was imposed at the distal adventitial layer. The parameters used for the numerical simulations are summarized in Table 1.

Table 1. Parameters in NV diffusion simulation.

Parameter	Symbol	Value
Blood density	ρ_{blood}	1060 kg/m³
Artery density	ρ_{artery}	1300 kg/m³
Zero-shear viscosity	μ_0	0.161 kg/(m·s)
Infinite-shear viscosity	μ_∞	0.0035 kg/(m·s)
Relaxation time	λ	39.418 s
Power-law index	n	0.479
NV diffusion coefficient	D	5.5×10^{-12} m²/s

A baseline diffusion coefficient of 5.5×10^{-12} m²/s was selected to reflect the physical transport characteristics of NVs with an average diameter of approximately 100–150 nm. This selection is consistent with established experimental and computational characterizations of microvesicles and drug-encapsulated nanoparticles in vascular environments [35, 75]. To account for uncertainty regarding the precise *in vivo* diffusion behavior of these NVs, a parametric study was performed using diffusion coefficients of 5.5×10^{-12}, 5.5×10^{-13}, and 5.5×10^{-14} m²/s. The primary parameters applied in the simulation are summarized in Table 1. The numerical solution was obtained using a pressure-based transient solver with the SIMPLE pressure-velocity coupling algorithm. Spatial discretization was performed using second-order schemes for pressure and momentum, and a first-order upwind scheme for transport.

Structural analysis of stent expansion

To evaluate the mechanical integrity and deformation behavior of the BRS during deployment, structural finite element analysis was performed using ANSYS Mechanical 2023 R1. The stent material, PLLA,

was modeled using an elasto-plastic material representation incorporating a multilinear isotropic hardening model to capture nonlinear post-yield behavior. The baseline mechanical properties assigned to the PLLA domain, adapted from Pauck and Reddy, included a density of 1250 kg/m^3, Young's modulus of 2300 MPa, Poisson's ratio of 0.43, and an initial tensile yield strength of 66.5 MPa [76]. The complete stress-strain curve defining the plastic deformation limits of the PLLA material model is presented in **Figure S12**.

To simulate the physical balloon-driven expansion process, a uniform outward radial pressure was applied to the inner luminal surfaces of the stent struts. The loading was ramped to a maximum internal pressure of 2.5 MPa, corresponding to 25 atm. Under these physiological loading conditions, the solver computed the resulting equivalent von Mises stress and plastic strain distributions. This analysis enabled characterization of the structural loading response and identification of localized regions undergoing permanent plastic deformation upon full expansion.

MSC-NV characterization

MSC-NV morphology was visually evaluated using TEM (JEM-F200, JEOL, Japan). MSC-NV size and concentration were determined via NTA using a NanoSight Pro (Malvern Panalytical, Worcestershire, United Kingdom; NFEC-2024-02-294501). dSTORM (Nanoimager S; ONI, Oxford, United Kingdom; NFEC-2025-09-308493) imaging was performed to characterize surface proteins on MSC-NVs, and tetraspanin markers CD9, CD63, and CD81 were labeled on the NV surface. miRNA expression was analyzed via microarray at Macrogen, Inc. (Seoul, Republic of Korea) using an Affymetrix GeneChip® miRNA 4.0 Array (*Homo sapiens*).

Cellular uptake of MSC-NVs

For hCAEC uptake time-course analysis, MSC-NVs were labeled with DiD (Thermo Fisher Scientific). Purified NVs were incubated with DiD for 30 min at 37 °C in the dark, centrifuged three times at 21,400 × g for 30 min each to remove unbound dye, and washed twice with DPBS. hCAECs were treated with 10 μg/mL DiD-labeled Fresh- or Lyo-NVs and fixed at 0, 0.5, 4, 8, and 24 h after incubation. Nuclei were stained with DAPI, and fluorescence images were acquired using a fluorescence microscope (ECLIPSE Ts2-FL, Nikon, Japan) under identical imaging conditions. Cell-associated DiD fluorescence was quantified using ImageJ, normalized to the number of DAPI-positive nuclei, and expressed relative to the mean fluorescence value at 0 h. For hAoSMC and PMA-induced THP-1 macrophage-like cell uptake analysis, MSC-NVs were labeled with DiO (Thermo Fisher Scientific). Purified NVs were incubated with DiO for 30 min at 37 °C in the dark, centrifuged three times at 21,400 × g for 30 min each to remove unbound dye, and washed twice with DPBS. Cells were treated with 10 μg/mL DiO-labeled MSC-NVs for 4 h. DiO-labeled NV uptake was analyzed using a confocal laser scanning microscope (LSM800 Airy, ZEISS, Germany) at the BT Research Facility Center, Chung-Ang University. For hAoSMCs, F-actin staining was performed using ReadyProbes™ Reagent F-Actin Phalloidin Conjugates (Invitrogen, Carlsbad, CA, USA), and fluorescence imaging was conducted using a fluorescence microscope (ECLIPSE Ts2-FL, Nikon, Japan). Additionally, an organ-on-a-chip system (MEPS-TBC-WL, pore size = 3 μm, PETE membrane; MEPSGEN, Seoul, Republic of Korea) assessed MSC-NV transendothelial transport. hCAECs, MSC-NVs, and hAoSMCs were labeled with DiD, DiO, and DiI, respectively.

Cellular uptake of DiI-labeled ox-LDL (DiI-ox-LDL)

THP-1 monocytes were differentiated into macrophages using 200 nM PMA for 48 h, followed by a 24 h resting period in RPMI-1640 medium supplemented with 10% FBS and 1% P/S. Subsequently, cells were starved for 24 h in DMEM/F-12 medium (Sigma-Aldrich) supplemented with 1% FBS and 1% P/S. Thereafter, cells were activated into M1 macrophages via incubation with 1 μg/mL LPS (Sigma-Aldrich) and 20 ng/mL IFN-γ for 24 h. Foam cell formation was induced via incubation with 10 μg/mL DiI-ox-LDL (Invitrogen) for an additional 24 h.

In vitro dose-response and cytocompatibility assays

Fresh- and Lyo-NVs were evaluated at 0.1, 1, 10, and 50 μg/mL. For hCAEC qRT-PCR and CCK-8 analyses, cells were stimulated with LPS (100 ng/mL) and treated with MSC-NVs for 6 h. For hAoSMC inflammatory-gene analysis, cells were stimulated with TNF-α and IFN-γ (10 ng/mL each) and treated with MSC-NVs for 6 h. For hAoSMC metabolic activity analysis, cells were stimulated with PDGF-BB (20 ng/mL) and treated with MSC-NVs for 48 h.

For each stimulation experiment, the first Saline group served as the non-stimulated vehicle control, whereas the second Saline group received the indicated stimulus without MSC-NV treatment. Fresh- and Lyo-NV groups received the same stimulus together with the corresponding MSC-NV formulation. The stimulated groups were identified by the horizontal stimulus bar in each figure.

Metabolic activity was evaluated using a CCK-8 kit (Dojindo, CK04). Following incubation with the CCK-8 reagent for 2 h, absorbance was measured at 450 nm using Multiskan GO microplate reader (Thermo Fisher Scientific). Live/Dead assays were performed separately in non-stimulated cultures treated with Fresh- or Lyo-NVs alone for 6 h using Live/Dead™ Cell Imaging Kit (Invitrogen, R37601). Live and dead cells were visualized as green and red fluorescence, respectively, using an ECLIPSE Ts2-FL fluorescence microscope (Nikon, Japan).

SMC phenotypic modulation

For SMC phenotypic analysis, hAoSMCs were stimulated with PDGF-BB (20 ng/mL), TNF-α (10 ng/mL), and IFN-γ (10 ng/mL) and treated with Fresh- or Lyo-NVs at 10 μg/mL. qRT-PCR and α-SMA immunofluorescence analyses were performed after 48 h, whereas cell migration was assessed over 10 h under the same combined-stimulation condition. The expression of *ACTA2*, *CNN1*, *TAGLN*, and *PDGFRB* was analyzed via qRT-PCR.

hBVAF activation assay

hBVAFs were stimulated with TGF-β1 (10 ng/mL) and treated with Fresh- or Lyo-NVs at 10 μg/mL for 48 h. Experimental groups comprised a non-stimulated Saline control, a TGF-β1-stimulated Saline vehicle control, and TGF-β1-stimulated Fresh- and Lyo-NV treatment groups. Fibroblast activation was evaluated via α-SMA immunofluorescence and qRT-PCR analysis of *ACTA2*, *TAGLN*, *POSTN*, *COL3A1*, and *FN1*.

Cell migration assay

Cells were seeded in 24-well plates at a density of 2×10^4 cells per well and cultured for 48 h until adequate confluency was reached. hCAEC migration was evaluated under LPS stimulation, whereas hAoSMC migration was evaluated under combined PDGF-BB, TNF-α, and IFN-γ stimulation, with or without the corresponding MSC-NV treatment. A scratch was created using a 200 μL micropipette tip, and detached cells were removed by DPBS washing before replacing the medium with the appropriate experimental medium. Cell migration was observed under a microscope equipped with a 10× objective lens, and the migrated area was quantified using ImageJ (version 1.54g; National Institutes of Health, Bethesda, MD, USA). For each biological replicate, three predefined fields of view along the scratch area were imaged at the same positions at each time point and used for quantification. The migration area was calculated as follows: (original scratch area) − (remaining scratch area). Following quantification, values were normalized to the non-stimulated Saline control group.

Immunofluorescence staining and analysis

Cells were washed with DPBS and fixed with 4% paraformaldehyde for 10 min at room temperature. A blocking solution was prepared by dissolving 250 mg bovine serum albumin and 30 μL Tween-20 (Sigma-Aldrich) in 5 mL DPBS, and cells were incubated with blocking solution at 4 °C for 1 h. Subsequently, cells were treated with the primary antibodies anti-VCAM-1 (Cat. No. ab134047; Abcam, Cambridge, United Kingdom; 1:250), anti-α-SMA (Cat. No. 14-9760-82; Invitrogen; 1:500), and anti-iNOS (Cat. No. ab3523; Abcam; 1:50) for 1 h at room temperature, followed by overnight incubation at 4 °C. Thereafter, secondary antibodies anti-mouse Alexa Fluor 488 (Cat. No. A-11001; Invitrogen; 1:1000), anti-rabbit Alexa Fluor 488 (Cat. No. A-11008; Invitrogen; 1:500), and anti-rabbit Alexa Fluor 568 (Cat. No. A-11011; Invitrogen; 1:500) were applied for 2 h at room temperature. Nuclear staining was performed using DAPI (Invitrogen; 1:3000). VCAM-1 expression was imaged using a confocal laser scanning microscope (LSM800 Airy), and α-SMA was visualized using a fluorescence microscope (ECLIPSE Ts2-FL). For *in vitro* immunofluorescence quantification, 1–3 randomly selected fields of view were imaged per biological replicate and used for analysis. For hAoSMC phenotypic analysis, α-SMA fiber organization was quantified using ImageJ-based image processing and orientation analysis and expressed as the relative anisotropy index. A total of 6 randomly selected non-overlapping fields were analyzed per biological replicate, and field-level measurements were averaged to generate one value per replicate. Values were normalized to the non-stimulated Saline control. For hBVAF analysis, a fixed fluorescence-intensity threshold was applied uniformly to all α-SMA images using ImageJ. The threshold-positive α-SMA area was normalized to the number of DAPI-positive nuclei in the same field and expressed as α-SMA-positive area per nucleus. A total of 6 randomly selected non-overlapping fields were analyzed per biological replicate, and field-level measurements were averaged to generate one value per replicate. For *in vivo* analysis, primary PDGFR-β (Cat. No. orb671428), CD31 (Cat. No. orb688857), and CD68 (Cat. No. orb735704) antibodies were obtained from Biorbyt (Durham, NC, USA), while VCAM-1 (Cat. No. BS-0920R) and α-SMA (Cat. No. BS-3418R) antibodies were obtained from Bioss (Woburn, MA, USA). Secondary antibodies, including anti-mouse Alexa Fluor 594 (Cat. No. 715-585-150), anti-goat Alexa Fluor 594 (Cat. No. 705-585-147), anti-mouse Alexa Fluor 488 (Cat. No. 715-545-

150), and anti-goat Alexa Fluor 488 (Cat. No. 705-545-147), were obtained from Jackson ImmunoResearch (Bar Harbor, ME, USA). DAPI was obtained from Vector Laboratories (Newark, CA, USA). Immunofluorescence analysis was performed on paraffin-embedded sections using primary antibodies stained against PDGFR-β, α-SMA, VCAM-1, CD68, and CD31. Samples were counterstained with DAPI to visualize cell nuclei. The degree of PDGFR-β-, α-SMA-, VCAM-1-, CD68-, and CD31-positive cell deposition was subjectively based on density and distribution around BRS struts as follows: 1, mild; 2, mild to moderate; 3, moderate; 4, moderate to severe; 5, severe. For *in vivo* immunofluorescence analysis, 10 randomly selected fields per sample were evaluated using CaseViewer software.

Quantitative real-time-PCR and RNA analysis

Total RNA was isolated from cells using the RNeasy Mini Kit (Qiagen, Hilden, Germany). Complementary DNA was synthesized using AccuPower® CycleScript RT Premix (Bioneer, Daejeon, Republic of Korea) according to the manufacturer's instructions. qRT-PCR was performed using SYBR Green Master Mix (Thermo Fisher Scientific) on a QuantStudio 1 Real-Time PCR system. Relative gene expression was calculated using the ΔΔCt method, normalized to glyceraldehyde-3-phosphate dehydrogenase (GAPDH) as the reference gene. Primers used in this experiment are listed in Table 2.

Table 2. List of primer sequences used for qRT-PCR.

Gene	Forward (5′→3′)	Reverse (3′→5′)
h*GAPDH*	ATGTTGCAACCGGGAAGGAA	GGAGCGCAGGGTTAGTCAC
h*IL1B*	GCTGCTCTGGGATTCTCTTCA	TGGCGAGCTCAGGTACTTCT
h*IL6*	TTCGGTCCAGTTGCCTTCTC	TCTTCTCCTGGGGGTACTGG
h*TNF*	AGTGCTGGCAACCACTAAGA	GATCAAAGCTGTAGGCCCCA
h*VCAM1*	TGACTTGCAGCACCACAGG	CACCTTCCCATTCAGTGGAC
h*ICAM1*	ACAACAGGCCCAAAAAGGGA	GATAGGTTCAGGGAGGCGTG
h*SELE*	GGTCCAGCTGTGAGTTCTCC	GCCACATTGGAGCCTTTTGG
h*IL13*	ATGCATCCGCTCCTCAATCC	AGTGAGAGCAATGACCGTGG
h*ACTA2*	GTTCCGCTCCTCTCTCCAAC	TGAAGCGGAAGTCTGGGAAG
h*CNN1*	CCAACGACCTGTTTGAGAACACC	ATTTCCGCTCCTGCTTCTCTGC
h*TAGLN*	TGTCCGAACCCAGACACAAG	CAGCCAATGCACTCACAAGG
h*PDGFRB*	TGCAGACATCGAGTCCTCCAAC	GCTTAGCACTGGAGACTCGTTG
h*POSTN*	AGGTCACCAAGGTCACCAAA	CTTCCTCACGGGTGTGTCTC
h*COL3A1*	CGCCCTCCTAATGGTCAAGG	CCAGGGTCACCATTTCTCCC
h*FN1*	TTCTGGTCAGCAACCCAGTG	TCTTGTCCTACATTCGGCGG

Small RNA sequencing and data processing

Small RNA libraries were prepared from MSC-NV samples (n = 3 biological replicates) using the NEBNext Small RNA Library Prep Set for Illumina and sequenced on an Illumina platform as 101-bp paired-end reads (Macrogen, Seoul, Republic of Korea). Raw sequencing reads were quality-filtered, adapter-trimmed (Cutadapt v4.4), and reads mapping to ribosomal RNA were removed. Processed reads were aligned to miRBase (release 22.1) precursor sequences using Bowtie (v1.1.2), and mature miRNA read counts were extracted using the miRDeep2 (v2.0.0.8) Quantifier module. Mature miRNA identifiers and raw read counts were used to construct the raw count matrix for all downstream analyses. miRNAs with a non-zero count in at least 2 of 3 samples were retained and normalized using the trimmed mean of M-values (TMM) method (edgeR v4.8.2), followed by log2(counts per million) transformation (prior count = 1). Sample quality and consistency across replicates were confirmed by pairwise Pearson correlation and principal component analysis (PCA) of log2(TMM-CPM) values.

miRNA target prediction and functional network analysis

For each miRNA, mean log2(TMM-CPM) expression was calculated across the three MSC-NV replicates, and the 50 miRNAs with the highest mean expression were selected for downstream analysis. Validated target genes of these miRNAs were retrieved from the multiMiR database (v1.32.0; "validated" table), restricted to interactions with strong experimental support (support type "Functional MTI" or "positive"); the same procedure was applied to all miRNAs detected in MSC-NV to define a background gene set. Over-representation of GO biological process terms among the target genes of the top 50 miRNAs, relative to this background, was tested with enrichGO (Benjamini–Hochberg-adjusted $p < 0.05$, $q < 0.2$, maximum gene-set size 250). Enriched GO biological process terms were classified into four mechanism categories relevant to vascular remodeling (endothelialization, VSMC activation, inflammation, and fibroblast activation) by keyword matching on term descriptions. A network linking the top 50 miRNAs, their target genes annotated to the enriched, mechanism-relevant GO terms, and the four mechanism categories was constructed and visualized; target genes shared by four or more of the top 50 miRNAs ("hub genes") were retained.

Endothelial tube formation

HUVECs were used for the tube formation assay instead of hCAECs owing to their robust and reproducible network formation on Matrigel under static culture conditions, enabling consistent assessment of CyA-induced endothelial dysfunction

and its recovery following MSC-NV treatment. Matrigel (Corning, NY, USA) was coated onto 24-well plates at 200 µL per well before seeding HUVECs. After seeding, HUVECs were incubated at 37 °C for 2 h to allow attachment to the Matrigel. CyA (Sigma-Aldrich), an inhibitor of endothelial cell function and tube formation, was added to each well at 25 µg/mL with or without MSC-NVs. After 12 h of treatment, cells were stained with calcein AM (Thermo Fisher Scientific) for visualization. Tubulogenesis was analyzed using a fluorescence microscope (ECLIPSE Ts2-FL) and quantified from acquired images using ImageJ (version 1.54g; National Institutes of Health).

Animal study design

Balloon injury was performed using a push–pull technique in the targeted iliac artery to establish a stenosis model in 16 male New Zealand white rabbits (JA BIO, Suwon, Gyeonggi-do, Republic of Korea), weighing 3.5–4.0 kg (mean weight, 3.84 kg). Rabbits were randomly divided into two groups (n = 6), receiving either bare BRS or NVE-BRS in the injured iliac artery 1 week after balloon-induced injury. The remaining four rabbits were used for specific experimental purposes: two rabbits, one normal and one balloon-injured, were used to validate establishment of the balloon-injury model before BRS implantation, whereas the other two rabbits received SRL-BRS for supplementary comparison analyses. The SRL-BRS group underwent the same balloon injury and BRS implantation procedures as the main experimental groups and was followed for 4 weeks after implantation. All 16 rabbits were maintained under the same housing and animal care conditions and were included under the same approved Institutional Animal Care and Use Committee (IACUC) of Asan Institute for Life Sciences protocol. MSC-NVs in NVE-BRS were fluorescently labeled with DiD (Thermo Fisher Scientific) for further visualization. After BRS placement, all animals received aspirin (40 mg/d; Bayer AG, Leverkusen, Germany) and clopidogrel (Plavix 75 mg, 4 mg/kg; HANDOK Inc., Seoul, Republic of Korea) according to standard treatment guidelines. The drugs were administered daily, starting from one day before BRS placement until sacrifice. Animals were housed at 24 ± 2 °C under a 12 h day/night cycle with free access to water and food. Rabbits were euthanized 4 weeks after BRS placement via potassium chloride overdose (by 75 mg/kg), to evaluate early vascular healing, including re-endothelialization, inflammatory responses, and neointimal remodeling following BRS implantation.

Balloon-induced injury model in the rabbit iliac artery

Rabbits were anesthetized using 50 mg/kg zolazepam, 50 mg/kg tiletamine (Zoletil 50; Virbac, Carros, France), and 10 mg/kg xylazine (Rompun; Bayer HealthCare). Thereafter, an endotracheal tube was placed and anesthesia was maintained via inhalation of 0.5–2% isoflurane (Ifran®; Hana Pharm. Co., Seoul, Republic of Korea) with a 1:1 oxygen concentration (510 mL/kg/min). The left common carotid artery was exposed via skin incision and punctured using an 18-Gauge angiocath. The angiocath was replaced with a 6-Fr sheath (Radifocus Introducer™; Terumo, Tokyo, Japan) under fluoroscopic guidance (OEC Elite CFD; GE HealthCare, Chicago, IL, USA). Heparin (100 U/kg; JW Pharm Co., Seoul, Republic of Korea) was administered through the sheath. A 0.035-inch guidewire (Radifocus®) with a 6-Fr guiding catheter (envoy®; Johnson & Johnson, New Brunswick, NJ, USA) was advanced into the common iliac artery. Pre-angiography measured the luminal diameter of the targeted iliac artery. A 3 mm diameter, 12 mm NC balloon catheter (NC TREK NEO™; Abbott, Illinois, USA) was used to induce iliac artery injury using a push-pull technique [77]. The balloon catheter was inflated with a mixture of contrast medium and saline to 10–12 atm, achieving a BRS-to-artery diameter ratio of 1.3 to induce vascular injury **(Figure S13)**. After the procedure, all catheters were removed, the incision was repaired and the animal was allowed to recover.

BRS placement into the balloon-injured iliac artery

After anesthesia in the same manner described above, a 0.014-inch micro-guidewire (Traxcess®; MicroVention, Aliso Viejo, CA, USA) with the 6-Fr guiding catheter was advanced into the balloon-injured iliac artery. Pre-angiography determined the location of BRS placement. The balloon catheter clamped with a BRS (2.5 mm diameter, 8 mm length, and 100 µm strut thickness) was inserted over the guidewire. The BRS was deployed at 8 atm using a pressure gauge, and post-angiography confirmed BRS patency and identified procedure-related adverse events **(Figure S14)**. Ketorolac tromethamine (1 mg/kg) (Hana Pharm Ltd.) and gentamicin (7 mg/kg) (Shin Poong Pharm Ltd., Seoul, Republic of Korea) were administered intramuscularly for 3 d to manage postoperative pain and infection.

Follow-up angiography and optical coherence tomography

Angiography and OCT (Aurios™; Dotter Inc., Yeonsu-gu, Incheon, Republic of Korea) were

performed immediately and at 4 weeks after BRS placement to assess BRS patency and complications. Luminal diameters from follow-up angiography were measured and compared between study groups using RadiAnt DICOM viewer (version 2020.2, Medixant Company, Poland). Luminal diameter changes were calculated using the following formula: Luminal diameter change (%) = [(luminal diameter at 4-weeks − immediate luminal diameter) / immediate luminal diameter] × 100. The OCT system and OCT imaging catheter (Benetis™; Dotter Inc., Yeonsu-gu, Incheon, Republic of Korea) were advanced distally into the target lesion via a 0.014-inch micro-guidewire. OCT catheter pullback was performed with contrast injection through the guiding catheter (with typical flush rates of 4.0–5.5 mL/s at 300–400 psi). Continuous cross-sections were analyzed at 180 μm longitudinal intervals with pullback speed adjustment according to validated methods [78-81]. Luminal diameters were measured at the middle segment of the stented iliac artery using the OCT software system. Ten cross-sections per segment were obtained to analyze neointimal thickness and SA. The percentage of SA was calculated using the formula: SA% = (neointimal area/stent area) × 100.

Histological analysis

Stented iliac arteries were surgically extracted after sacrifice. Both iliac arteries were flushed with heparinized saline and samples were fixed in 10% formaldehyde. Stented segments were embedded in paraffin and sectioned into 5 μm-thick slices. Samples were subsequently stained with H&E, MT, and VVG. Histological evaluation using H&E staining determined the degree of inflammatory cell infiltration and fibrin deposition. The degree of collagen deposition was determined in MT-stained sections. The degree of inflammatory cell infiltration, fibrin deposition, and collagen deposition were evaluated according to the density and distribution around BRS struts as follows: 1, mild; 2, mild to moderate; 3, moderate; 4, moderate to severe; and 5, severe [82-84]. VVG staining evaluated changes in the EL. EL changes were classified into three grades: 0 = no injury; 1 = break in the internal elastic membrane; 2 = media perforation; 3 = perforation of the external elastic membrane extending to the adventitia [78, 85]. All stained samples were scanned using a digital slide scanner (Panoramic 250 FLASH III; 3D Histech Ltd., Budapest, Hungary). Slides were analyzed using CaseViewer (3D Histech Ltd.) by evaluating 10 randomly selected fields for statistical reliability.

Statistical analyses

Data are presented as the mean ± standard deviation (SD). For comparisons between two groups, normally distributed continuous variables were analyzed using an unpaired two-tailed Student's t-test, whereas non-normally distributed data were analyzed using the Mann–Whitney U test. For comparisons among multiple groups, one-way analysis of variance (ANOVA) followed by Tukey's post hoc test was used for normally distributed data, whereas the Kruskal–Wallis test with Dunn's post hoc test was used for non-normally distributed data. A p value < 0.05 was considered statistically significant. Statistical significance is indicated as follows: ns, not significant; *p < 0.05; **p < 0.01; ***p < 0.001, and ****p < 0.0001. Statistical analyses were performed using SPSS (version 28.0; IBM, Chicago, USA) and GraphPad Prism (version 10.3.1; La Jolla, CA, USA).

Abbreviations

ANOVA: analysis of variance; BCA: bicinchoninic acid; BMS: bare-metal stent; BRS: bioresorbable scaffold; CABG: coronary artery bypass grafting; CyA: cyclosporin A; DAPI: 4′,6-diamidino-2-phenylindole; DES: drug-eluting stent; DiD: 1,1′-dioctadecyl-3,3,3′,3′-tetramethylindodicarbocyanine; DiI: 1,1′-dioctadecyl-3,3,3′,3′-tetramethylindocarbocyanine; DiO: 3,3′-dioctadecyloxacarbocyanine perchlorate; DMEM: Dulbecco's modified Eagle's medium; DPBS: Dulbecco's phosphate-buffered saline; dSTORM: direct stochastic optical reconstruction microscopy; EC: endothelial cell; EL: elastic lamina; EV: extracellular vesicle; F-actin: filamentous actin; FBS: fetal bovine serum; GAPDH: glyceraldehyde-3-phosphate dehydrogenase; H&E: hematoxylin and eosin; hAoSMC: human aortic smooth muscle cell; hASC: human adipose-derived stem cell; hCAEC: human coronary artery endothelial cell; HUVEC: human umbilical vein endothelial cell; IACUC: Institutional Animal Care and Use Committee; ICAM-1: intercellular adhesion molecule-1; IFN-γ: interferon-γ; IL: interleukin; iNOS: inducible nitric oxide synthase; LPS: lipopolysaccharide; miRNA: microRNA; MSC: mesenchymal stem cell; MSC-NV: mesenchymal stem cell-derived nanovesicle; MT: Masson's trichrome; NTA: nanoparticle tracking analysis; NV: nanovesicle; NVE-BRS: nanovesicle-eluting bioresorbable scaffold; OCT: optical coherence tomography; ox-LDL: oxidized low-density lipoprotein; PCI: percutaneous coronary intervention; PDGF-BB: platelet-derived growth factor-BB; PDGFR-β: platelet-derived growth factor receptor-β; PLLA: poly(L-lactic acid); PMA: phorbol 12-myristate 13-acetate; PMB30W: poly(2-methacryloyloxyethyl phosphorylcholine-co-n-butyl methacrylate); P/S: penicillin-streptomycin; qRT-PCR: quantitative real-

time polymerase chain reaction; SA: stenosis area; SD: standard deviation; SMC: smooth muscle cell; SRL-BRS: sirolimus-eluting bioresorbable scaffold; TEM: transmission electron microscopy; TNF-α: tumor necrosis factor-α; VCAM-1: vascular cell adhesion molecule-1; VSMC: vascular smooth muscle cell; VVG: Verhoeff-Van Gieson; α-SMA: α-smooth muscle actin.

Supplementary Material

Supplementary figures and table 1.
https://www.thno.org/v17p0524s1.pdf
Supplementary tables 2-5.
https://www.thno.org/v17p0524s2.xlsx

Acknowledgements

This study was financially supported by i) Technology Innovation Program (RS-2024-00448758) funded by the Ministry of Trade, Industry and Energy (MOTIE), Republic of Korea, ii) National Research Foundation of Korea (NRF) grant funded by the Korea government (MSIT) (RS-2023-00213691, 2021K1A3A1A74099704, RS-2026-25469139), iii) Korean Fund for Regenerative Medicine (KFRM) grant funded by the Korea government (the Ministry of Science and ICT, the Ministry of Health & Welfare) (KFRM 25A0105L1), iv) Korea Basic Science Institute (National research Facilities and Equipment Center) grant funded by the Ministry of Science and ICT (RS-2025-00562624), v) the Korea Evaluation Institute of Industrial Technology (KEIT) grant funded by the Korea government (MSIT) (20023041), and vi) the ANCHOR program through the Gangwon ANCHOR Center, funded by the Ministry of Education(MOE) and the Gangwon State(G.S.), Republic of Korea (2026-ANCHOR-10-002).

Author contributions

Min-Kyu Kang: Investigation, Data curation, Validation, Visualization, Writing – original draft. Ji Won Kim: Investigation, Data curation, Validation, Visualization, Writing – original draft. Yu-Jeong Lee: Investigation, Data curation, Formal analysis, Validation, Visualization, Writing – original draft. Dong-Sung Won: Investigation, Validation. Gi Wook Lee: Resources. Weiqiang Liu: Software, Investigation, Writing – original draft. Chae-lin Kim: Formal analysis, Bioinformatics, Visualization, Writing – original draft. Su-Hyun Park: Investigation. Ju-El Kim: Investigation. Tae-Hyun Heo: Investigation. Seung Jin Eo: Investigation. Gun-Jae Jeong: Investigation, Writing – original draft. Ilkoo Noh: Data interpretation, Writing – review & editing. Min-Ho Kang: Investigation, Writing – original draft. Han Young Kim: Investigation, Writing – original draft. Jung Bok Lee: Investigation, Writing – original draft. Young Min Shin: Data interpretation, Writing – review & editing. Minseo Park: Formal analysis, Bioinformatics, Visualization. Hyun-Ji Park: Formal analysis, Bioinformatics, Visualization, Writing – review & editing. Rosaire Mongrain: Investigation, Writing – original draft. Hyung Il Kim: Resources. Jung-Hoon Park: Supervision, Project administration, Funding acquisition, Writing – review & editing. Jeong-Kee Yoon: Conceptualization, Supervision, Funding acquisition, Project administration, Writing – review & editing.

Data availability

The data supporting this study are available from the corresponding author upon reasonable request.

Ethics approval statement

Following the US National Institutes of Health's recommendations for the humane treatment of laboratory animals, this study was approved by the Institutional Animal Care and Use Committee of Asan Institute for Life Sciences (IACUC approval number: 2023-20-216).

Competing Interests

The authors have declared that no competing interest exists.

References

1. Han Y, Xu H, Yao X, Li Z, Zhu C, Li X, et al. Molecular mechanisms and therapeutic progress in atherosclerosis: bridging immune inflammation and precision medicine. Front Immunol. 2025; 16: 1737662.
2. Zeng R-X, Li S, Li J-J. Cholesterol-inflammation fusion hypothesis in atherosclerosis: an evolving paradigm in pathogenesis and therapy. JACC Asia. 2026; 6: 284–96.
3. Wang K, Yin Z, Zhang Y, Wu X, Fan L. From bench to clinic: advances in anti-inflammatory therapies for atherosclerotic coronary artery disease. FASEB J. 2025; 39: e71056.
4. Morrison AM, Sullivan AE, Aday AW. Atherosclerotic disease: pathogenesis and approaches to management. Med Clin North Am. 2023; 107: 793–805.
5. Liberale L, Montecucco F, Tardif J-C, Libby P, Camici GG. Inflamm-ageing: the role of inflammation in age-dependent cardiovascular disease. Eur Heart J. 2020; 41: 2974–82.
6. Kang M-K, Heo S-H, Yoon J-K. In-stent re-endothelialization strategies: cells, extracellular matrix, and extracellular vesicles. Tissue Eng Part B Rev. 2025; 31: 317–30.
7. Huang Z, Skarbek C, Li Y, Touma J, Desgranges P, Gallet R, et al. Evolution of coronary stents: from birth to future trends. J Clin Med. 2025; 15: 47.
8. Arh R, Balevski I, Granda S, Bevc S. Drug-eluting stent use in percutaneous coronary interventions—a narrative review. J Clin Med. 2025; 14: 4643.
9. Zong J, He Q, Liu Y, Qiu M, Wu J, Hu B. Advances in the development of biodegradable coronary stents: a translational perspective. Mater Today Bio. 2022; 16: 100368.
10. Dinc R, Ardic N. Extracellular vesicles as biological templates for next-generation drug-coated cardiovascular devices: cellular mechanisms of vascular healing, inflammation, and restenosis. Cells. 2026; 15: 121.
11. Jin YJ, Park DS, Jeong MH, Sim DS, Na MH, Kim CW, et al. Dual-drug stent with sirolimus and WKYMVm promotes endothelialization and limits hyperplasia. Tissue Eng Regen Med. 2026: 1–14.
12. Bourazana A, Briasoulis A, Kourek C, Kuno T, Leventis I, Pantsios C, et al. Bioresorbable scaffolds for coronary revascularization: from concept to clinical maturity. J Cardiovasc Dev Dis. 2025; 13: 2.
13. Ding Y, Warlick L, Chen M, Taddese E, Collins C, Fu R, et al. 3D-printed, citrate-based bioresorbable vascular scaffolds for coronary artery angioplasty. Bioact Mater. 2024; 38: 195–206.
14. Wang C, Lv J, Yang M, Fu Y, Wang W, Li X, et al. Recent advances in surface functionalization of cardiovascular stents. Bioact Mater. 2025; 44: 389–410.

15. Yang S, Li K, Wang N, Li Z, Zhang Z, Tuan RS, et al. Engineering approaches to modify immunomodulatory functions of mesenchymal stromal cells (MSCs): tissue regeneration and clinical application. Adv Sci (Weinh). 2026: e22601.
16. Sarsenova M, Kim Y, Raziyeva K, Kazybay B, Ogay V, Saparov A. Recent advances to enhance the immunomodulatory potential of mesenchymal stem cells. Front Immunol. 2022; 13: 1010399.
17. Guan A, Alibrandi L, Verma E, Sareen N, Guan Q, Lionetti V, et al. Clinical translation of mesenchymal stem cells in ischemic heart failure: challenges and future perspectives. Vascul Pharmacol. 2025; 159: 107491.
18. Park J, Lee J, Kim Y-S, Oh Y. Proteomic profiling of exosomes derived from endometrial stem cells and adipose-derived stem cells. Int J Stem Cells. 2026; 19: 102–12.
19. Shi P, Ren C, Tong H. Research progress of stem cells in the treatment of atherosclerosis. Front Cell Dev Biol. 2025; 13: 1722416.
20. Gao Y-F, Zhao N, Hu C-H. Harnessing mesenchymal stem/stromal cells-based therapies for rheumatoid arthritis: mechanisms, clinical applications, and microenvironmental interactions. Stem Cell Res Ther. 2025; 16: 379.
21. Pandey SN, Afzal M, Goyal K, MM R, Nayak PP, Maqbool M, et al. The role of MSC-derived exosomes in immune modulation and regenerative medicine. J Drug Target. 2026: 1–35.
22. Pang J-L, Shao H, Xu X-G, Lin Z-W, Chen X-Y, Chen J-Y, et al. Targeted drug delivery of engineered mesenchymal stem/stromal-cell-derived exosomes in cardiovascular disease: recent trends and future perspectives. Front Bioeng Biotechnol. 2024; 12: 1363742.
23. Yadav S, Maity P, Kapat K. The opportunities and challenges of mesenchymal stem cells-derived exosomes in theranostics and regenerative medicine. Cells. 2024; 13: 1956.
24. Kim JH, Kim J-E, Kang S-J, Yoon J-K. Exosomes and exosome-mimetics for atopic dermatitis therapy. Tissue Eng Regen Med. 2025; 22: 381–96.
25. Jiang Y, Yu M, Song Z-F, Wei Z-Y, Huang J, Qian H-Y. Targeted delivery of mesenchymal stem cell-derived bioinspired exosome-mimetic nanovesicles with platelet membrane fusion for atherosclerotic treatment. Int J Nanomedicine. 2024; 19: 2553–71.
26. Yoon JK, Kim DH, Kang ML, Jang HK, Park HJ, Lee JB, et al. Anti-atherogenic effect of stem cell nanovesicles targeting disturbed flow sites. Small. 2020; 16: 2000012.
27. Kang WY, Shin EK, Kim EH, Kang M-H, Bang CY, Bang OY, et al. Lyoprotectant constituents suited for lyophilization and reconstitution of stem-cell-derived extracellular vesicles. Biomater Res. 2024; 28: 0005.
28. Lee YJ, Park M, Kim HY, Kim J-K, Kim W-K, Lim SC, et al. Circulating small extracellular vesicles promote proliferation and migration of vascular smooth muscle cells via AXL and MerTK activation. Acta Pharmacol Sin. 2023; 44: 984–98.
29. Zou X, Liao Y, Liu Z, Xu X, Sun W, Qin H, et al. Exosomes derived from AT2R-overexpressing BMSC prevent restenosis after carotid artery injury by attenuating the injury-induced neointimal hyperplasia. J Cardiovasc Transl Res. 2023; 16: 112–26.
30. Hu S, Li Z, Shen D, Zhu D, Huang K, Su T, et al. Exosome-eluting stents for vascular healing after ischaemic injury. Nat Biomed Eng. 2021; 5: 1174–88.
31. Duan L, He Y, Wu H, Li T, Liang J, Jia R, et al. Preparation of ROS-responsive exosome coating of nitinol material for making the neurointerventional stent. Adv Mater Interfaces. 2023; 10: 2300028.
32. Lee I, Kobayashi K, Sun H, Takatani S, Zhong L. Biomembrane mimetic polymer poly (2-methacryloyloxyethyl phosphorylcholine-co-n-butyl methacrylate) at the interface of polyurethane surfaces. J Biomed Mater Res A. 2007; 82: 316–22.
33. Tamura K, Kikuchi E, Konno T, Ishihara K, Matsumoto K, Miyajima A, et al. Therapeutic effect of intravesical administration of paclitaxel solubilized with poly (2-methacryloyloxyethyl phosphorylcholine-co-n-butyl methacrylate) in an orthotopic bladder cancer model. BMC Cancer. 2015; 15: 317.
34. Ishihara K. Biomimetic polymers with phosphorylcholine groups as biomaterials for medical devices. Proc Jpn Acad Ser B Phys Biol Sci. 2024; 100: 579–606.
35. Hossain SS, Hossainy SF, Bazilevs Y, Calo VM, Hughes TJ. Mathematical modeling of coupled drug and drug-encapsulated nanoparticle transport in patient-specific coronary artery walls. Comput Mech. 2012; 49: 213–42.
36. Liu H-T, Li F, Wang W-Y, Li X-J, Liu Y-M, Wang R-A, et al. Rapamycin inhibits re-endothelialization after percutaneous coronary intervention by impeding the proliferation and migration of endothelial cells and inducing apoptosis of endothelial progenitor cells. Tex Heart Inst J. 2010; 37: 194–201.
37. Moss SC, Lightell DJ, Marx SO, Marks AR, Woods TC. Rapamycin regulates endothelial cell migration through regulation of the cyclin-dependent kinase inhibitor p27Kip1. J Biol Chem. 2010; 285: 11991–7.
38. Chen J, Zhou C, Fang W, Yin J, Shi J, Ge J, et al. Identification of endothelial protein C receptor as a novel druggable agonistic target for reendothelialization promotion and thrombosis prevention of eluting stent. Bioact Mater. 2024; 41: 485–98.
39. Owens GK, Kumar MS, Wamhoff BR. Molecular regulation of vascular smooth muscle cell differentiation in development and disease. Physiol Rev. 2004; 84: 767–801.
40. Raines EW. PDGF and cardiovascular disease. Cytokine Growth Factor Rev. 2004; 15: 237–54.
41. Zhou D, Ha HC, Yang G, Jang JM, Park BK, Fu Z, et al. Hyaluronic acid and proteoglycan link protein 1 suppresses platelet-derived growth factor-BB-induced proliferation, migration, and phenotypic switching of vascular smooth muscle cells. BMB Rep. 2023; 56: 445–50.
42. Shi Y, O'Brien JE, Ala-Kokko L, Chung W, Mannion JD, Zalewski A. Origin of extracellular matrix synthesis during coronary repair. Circulation. 1997; 95: 997–1006.
43. Shi Y, O'Brien JE, Fard A, Mannion JD, Wang D, Zalewski A. Adventitial myofibroblasts contribute to neointimal formation in injured porcine coronary arteries. Circulation. 1996; 94: 1655–64.
44. Wang D, Gao B, Yue J, Liu F, Liu Y, Fu W, et al. Exosomes from mesenchymal stem cells expressing miR-125b inhibit neointimal hyperplasia via myosin IE. J Cell Mol Med. 2019; 23: 1528–40.
45. Selvakumar PP, Rafuse MS, Johnson R, Tan W. Applying principles of regenerative medicine to vascular stent development. Front Bioeng Biotechnol. 2022; 10: 826807.
46. Sprague AH, Khalil RA. Inflammatory cytokines in vascular dysfunction and vascular disease. Biochem Pharmacol. 2009; 78: 539–52.
47. Theofilis P, Sagris M, Oikonomou E, Antonopoulos AS, Siasos G, Tsioufis C, et al. Inflammatory mechanisms contributing to endothelial dysfunction. Biomedicines. 2021; 9: 781.
48. Buszman PP, Kachel M, Łukasik K, Nożyński J, Skowronek R, Grajek M, et al. Improved vascular response to a novel polymeric blend PLLA/PLGA coronary scaffold material: preclinical study. Sci Rep. 2025; 15: 34219.
49. Joner M, Ruppelt P, Zumstein P, Lapointe-Corriveau C, Leclerc G, Bulin A, et al. Preclinical evaluation of degradation kinetics and elemental mapping of first- and second-generation bioresorbable magnesium scaffolds. EuroIntervention. 2018; 14: e1040–8.
50. Bian X, Ma K, Zhang C, Fu X. Therapeutic angiogenesis using stem cell-derived extracellular vesicles: an emerging approach for treatment of ischemic diseases. Stem Cell Res Ther. 2019; 10: 158.
51. Virmani R, Kolodgie F, Farb A, Lafont A. Drug eluting stents: are human and animal studies comparable? Heart. 2003; 89: 133–8.
52. Schwartz RS, Edelman E, Virmani R, Carter A, Granada JF, Kaluza GL, et al. Drug-eluting stents in preclinical studies: updated consensus recommendations for preclinical evaluation. Circ Cardiovasc Interv. 2008; 1: 143–53.
53. Lee JM, Lee J, Jeong H, Choe WS, Seo W-W, Lim W-H, et al. Development of a rabbit model for a preclinical comparison of coronary stent types in-vivo. Korean Circ J. 2013; 43: 713–22.
54. Joner M, Nakazawa G, Finn AV, Quee SC, Coleman L, Acampado E, et al. Endothelial cell recovery between comparator polymer-based drug-eluting stents. J Am Coll Cardiol. 2008; 52: 333–42.
55. Onuma Y, Serruys PW. Bioresorbable scaffold: the advent of a new era in percutaneous coronary and peripheral revascularization? Circulation. 2011; 123: 779–97.
56. van Ditzhuijzen NS, Kurata M, van den Heuvel M, Sorop O, van Duin RW, Krabbendam-Peters I, et al. Neoatherosclerosis development following bioresorbable vascular scaffold implantation in diabetic and non-diabetic swine. PLoS One. 2017; 12: e0183419.
57. Bengueddache S, Cook M, Lehmann S, Arroyo D, Togni M, Puricel S, et al. Ten-year clinical outcomes of everolimus- and biolimus-eluting coronary stents vs. everolimus-eluting bioresorbable vascular scaffolds—insights from the EVERBIO-2 trial. Front Cardiovasc Med. 2024; 11: 1426348.
58. Inoue T, Croce K, Morooka T, Sakuma M, Node K, Simon DI. Vascular inflammation and repair: implications for re-endothelialization, restenosis, and stent thrombosis. JACC Cardiovasc Interv. 2011; 4: 1057–66.
59. Bedair TM, ElNaggar MA, Joung YK, Han DK. Recent advances to accelerate re-endothelialization for vascular stents. J Tissue Eng. 2017; 8: 2041731417731546.
60. Ochijewicz D, Tomaniak M, Opolski G, Kochman J. Inflammation as a determinant of healing response after coronary stent implantation. Int J Cardiovasc Imaging. 2021; 37: 791–801.
61. Lau HC, Han DW, Park J, Lehner E, Kals C, Arzt C, et al. GMP-compliant manufacturing of biologically active cell-derived vesicles produced by extrusion technology. J Extracell Biol. 2022; 1: e70.
62. Welsh JA, Goberdhan DCI, O'Driscoll L, Buzas EI, Blenkiron C, Bussolati B, et al. Minimal information for studies of extracellular vesicles (MISEV2023): from basic to advanced approaches. J Extracell Vesicles. 2024; 13: e12404.
63. Kuehbacher A, Urbich C, Zeiher AM, Dimmeler S. Role of Dicer and Drosha for endothelial microRNA expression and angiogenesis. Circ Res. 2007; 101: 59–68.
64. Fang Y, Shi C, Manduchi E, Civelek M, Davies PF. MicroRNA-10a regulation of proinflammatory phenotype in athero-susceptible endothelium in vivo and in vitro. Proc Natl Acad Sci U S A. 2010; 107: 13450–5.
65. Weber M, Baker MB, Moore JP, Searles CD. MiR-21 is induced in endothelial cells by shear stress and modulates apoptosis and eNOS activity. Biochem Biophys Res Commun. 2010; 393: 643–8.
66. Cordes KR, Sheehy NT, White MP, Berry EC, Morton SU, Muth AN, et al. miR-145 and miR-143 regulate smooth muscle cell fate and plasticity. Nature. 2009; 460: 705–10.
67. Yang F, Chen Q, He S, Yang M, Maguire EM, An W, et al. miR-22 is a novel mediator of vascular smooth muscle cell phenotypic modulation and neointima formation. Circulation. 2018; 137: 1824–41.
68. Iaconetti C, De Rosa S, Polimeni A, Sorrentino S, Gareri C, Carino A, et al. Down-regulation of miR-23b induces phenotypic switching of vascular smooth muscle cells in vitro and in vivo. Cardiovasc Res. 2015; 107: 522–33.

69. Zhu Z-R, He Q, Wu W-B, Chang G-Q, Yao C, Zhao Y, et al. MiR-140-3p is involved in in-stent restenosis by targeting C-Myb and BCL-2 in peripheral artery disease. J Atheroscler Thromb. 2018; 25: 1168–81.
70. Van Rooij E, Sutherland LB, Thatcher JE, DiMaio JM, Naseem RH, Marshall WS, et al. Dysregulation of microRNAs after myocardial infarction reveals a role of miR-29 in cardiac fibrosis. Proc Natl Acad Sci U S A. 2008; 105: 13027–32.
71. Zeng X, Huang C, Senavirathna L, Wang P, Liu L. miR-27b inhibits fibroblast activation via targeting TGFβ signaling pathway. BMC Cell Biol. 2017; 18: 9.
72. Banerjee S, Xie N, Cui H, Tan Z, Yang S, Icyuz M, et al. MicroRNA let-7c regulates macrophage polarization. J Immunol. 2013; 190: 6542–9.
73. Poulton J. Enhancing medication delivery of eluting stents: a computationally aided parametric approach. Montreal, Canada: McGill University; 2024.
74. Kwon O, Krishnamoorthy M, Cho YI, Sankovic JM, Banerjee RK. Effect of blood viscosity on oxygen transport in residual stenosed artery following angioplasty. J Biomech Eng. 2008; 130: 011003.
75. Kastelowitz N, Yin H. Exosomes and microvesicles: identification and targeting by particle size and lipid chemical probes. Chembiochem. 2014; 15: 923–8.
76. Pauck R, Reddy B. Computational analysis of the radial mechanical performance of PLLA coronary artery stents. Med Eng Phys. 2015; 37: 7–12.
77. Vorpahl M, Nakano M, Perkins L, Otsuka F, Jones R, Acampado E, et al. Vascular healing and integration of a fully bioresorbable everolimus-eluting scaffold in a rabbit iliac arterial model. EuroIntervention. 2014; 10: 833–41.
78. Kim JW, Won D-S, Eo SJ, Kim SH, Park Y, Kang D-Y, et al. Minimally overlapping technique of bioresorbable scaffolds in a porcine coronary artery model: proof-of-concept study. Sci Rep. 2025; 15: 38913.
79. Farooq V, Serruys PW, Heo JH, Gogas BD, Onuma Y, Perkins LE, et al. Intracoronary optical coherence tomography and histology of overlapping everolimus-eluting bioresorbable vascular scaffolds in a porcine coronary artery model: the potential implications for clinical practice. JACC Cardiovasc Interv. 2013; 6: 523–32.
80. Gutierrez-Chico JL, Van Geuns RJ, Regar E, Van Der Giessen WJ, Kelbæk H, Saunamäki K, et al. Tissue coverage of a hydrophilic polymer-coated zotarolimus-eluting stent vs. a fluoropolymer-coated everolimus-eluting stent at 13-month follow-up: an optical coherence tomography substudy from the RESOLUTE All Comers trial. Eur Heart J. 2011; 32: 2454–63.
81. Gutiérrez-Chico JL, Regar E, Nüesch E, Okamura T, Wykrzykowska J, di Mario C, et al. Delayed coverage in malapposed and side-branch struts with respect to well-apposed struts in drug-eluting stents: in vivo assessment with optical coherence tomography. Circulation. 2011; 124: 612–23.
82. Ryu DS, Won D-S, Kim JW, Park Y, Kim SH, Kang JM, et al. Efficacy of closed cell self expandable metallic stent for peripheral arterial disease in the porcine iliac artery. Sci Rep. 2023; 13: 8601.
83. Park J-H, Cho YK, Her K, Jeon YS, Kim JH, Seo T-S, et al. Histologic analysis with the newly designed exoskeleton Seal® stent-graft in the porcine abdominal aorta. Cardiovasc Intervent Radiol. 2019; 42: 1331–42.
84. Ryu DS, Won D-S, Kim JW, Park Y, Kim SH, Kang JM, et al. Efficacy of thermoplastic polyurethane and gelatin blended nanofibers covered stent graft in the porcine iliac artery. Sci Rep. 2022; 12: 16524.
85. Schwartz RS, Huber KC, Murphy JG, Edwards WD, Camrud AR, Vlietstra RE, et al. Restenosis and the proportional neointimal response to coronary artery injury: results in a porcine model. J Am Coll Cardiol. 1992; 19: 267–74.